



Ben-Gurion University of the Negev
The Faculty of Natural Sciences
The Department of **Physics**

Monte Carlo study of LiHoF_4 in a weak transverse magnetic field

Tomer Dollberg

Thesis submitted in partial fulfillment of the requirements
for the Master of Sciences degree

Under the supervision of **Prof. Moshe Schechter**

January 2020



אוניברסיטת בן-גוריון בנגב
הפקולטה למדעי הטבע
המחלקה לפיסיקה

מחקר בשיטת מונטה קרלו של LiHoF_4 תחת שדה מגנטי חלש

תומר דולברג

חיבור לשם קבלת התואר "מגיסטר" בפקולטה למדעי הטבע

בהנחיית פרופ' משה שכטר

טבת תש"פ



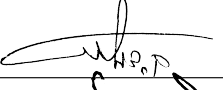
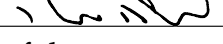

Ben-Gurion University of the Negev
The Faculty of Natural Sciences
The Department of **Physics**

Monte Carlo study of LiHoF_4 in a weak transverse magnetic field

Tomer Dollberg

Thesis submitted in partial fulfillment of the requirements
for the Master of Sciences degree

Under the supervision of **Prof. Moshe Schechter**

Signature of student:  Date: 29/01/2020
Signature of supervisor:  Date: 29/01/2020
Signature of chairperson of the
committee for graduate studies:  Date: 29/01/2020

January 2020

תקציר

LiHoF_4 הוא מגנט קוונטי הידוע כמימוש פיזיקלי של מודל איזינג תחת שדה אנכי עם אינטראקציות דיפולריות [1]. תוצאות ממחקרים קודמים, שהשתמשו בשיטות מונטה קרלו שונות [2, 3] וניתוחים המבוססים על תורת שדה ממוצע (Mean Field) [4, 5], הראו חוסר התאמה ביחס לתוצאות הניסיוניות בדיאגרמת הפאזות $B_x - T$ [1, 5, 6]. בפרט, בתחום של שדה אנכי חלש, קו מעבר הפאזה שנמדד בניסוי, המפריד בין הפאזה הפרומגנטית לפאזה הפאראמגנטית, תלוי בשדה החיצוני באופן חלש בהרבה ביחס לתחזיות התיאורטיות. בתזה זו אנחנו מציעים מנגנון שיכול להסביר את חוסר ההתאמה הזה. איברים לא-אלכסוניים של האינטראקציה הדיפולרית, שהשפעתם גדולה יותר בפאזה הפאראמגנטית, מקטינים את האנרגיה של פאזה זו, וכתוצאה מכך מקטינים את הטמפרטורה הקריטית. על ידי שימוש בסימולציות מונטה קרלו קלאסיות, בהן אנחנו מתייחסים במפורש לשינוי של מצבי איזינג הנגרם בהשפעת האיברים הלא-אלכסוניים, אנחנו מראים שלקחתם בחשבון מקטינה את הטמפרטורה הקריטית באופן משמעותי בהיעדר שדה מגנטי חיצוני. בנוסף, אנחנו מראים שההשפעה של המנגנון הזה נחלשת עם הוספת שדה מגנטי אנכי חיצוני, מה שיכול להסביר את התלות של הטמפרטורה הקריטית בשדה המגנטי.

Abstract

LiHoF₄ is a quantum magnet known to be a good physical realization of the transverse field Ising model with dipolar interactions [1]. Results from previous studies, using various Monte Carlo techniques [2, 3] and mean-field analyses [4, 5], show a persistent discrepancy with experimental results for the $B_x - T$ phase diagram [1, 5, 6]. Namely, in the low B_x regime, the experimental phase boundary separating the ferromagnetic and paramagnetic phases has a much smaller dependence on magnetic field in comparison to the theoretical predictions. In this work we propose a mechanism which may account for the discrepancy. Offdiagonal terms of the dipolar interaction, more dominant in the disordered paramagnetic phase, reduce the energy of the paramagnetic phase, and consequently reduce the critical temperature. Using classical Monte Carlo simulations, in which we explicitly take the modification of the Ising states due to the offdiagonal terms into account, we show that the inclusion of these terms reduces T_c markedly at zero transverse field. We also show that the effect is diminished with increasing transverse field, leading to the above mentioned field dependence of the critical temperature.

Acknowledgements

First, I would like to thank my supervisor, Moshe Schechter, for his help and guidance with this work. I am very grateful for his valuable advice, his patience and support, and for the knowledge he shared with me from which I benefited greatly.

I also want to express my gratitude to Juan Carlos Andresen Eguiluz for his professional guidance in the field of computational physics. His expertise proved essential to this work, and I consider myself fortunate having had the opportunity to learn from him. I would like to further thank him for being so readily available for discussions, much of them on his free time.

I would like to thank my parents for their love and support.

Lastly, I want to thank my girlfriend, Maayan, for her never ending support and patience which were invaluable to me during this time.

Contents

1	Introduction	1
1.1	LiHoF ₄	1
1.2	Transverse Field Ising Model	3
1.3	Outline	5
2	Theory	6
2.1	Crystal Structure and Microscopic Hamiltonian of LiHoF ₄	6
2.2	Mean-Field Solution	8
2.3	Effective Spin- $\frac{1}{2}$ Hamiltonian for LiHoF ₄	10
2.4	Nearest-Neighbor Exchange Interactions	12
2.5	Proposed Hamiltonian	14
3	Numerical Methods	18
3.1	Diagonalization of the single-site Hamiltonian	18
3.2	Self-consistent calculation	20
3.2.1	Nonlinear Gauss-Seidel method	21
3.2.2	Newton's and Broyden's methods	21
3.3	Monte Carlo simulation	23
3.3.1	Equilibration	24
3.3.2	Autocorrelation	26
3.3.3	Finite size scaling	28
4	Results	31

4.1 Discussion	35
5 Summary	38
A Single Ho³⁺ Ion and Crystal properties	40
A.1 Single Ion Electronic States	40
A.2 Crystal Field Hamiltonian	40
B Ewald Summation Method	44
C Interpolation	47
D Numerical Parameters	49

List of Figures

1.1	Low- B_x phase diagram of LiHoF ₄	3
1.2	Mean field phase diagram of TFIM	4
2.1	Unit cell structure of LiHoF ₄	7
2.2	$B_x - T_c$ phase diagram of LiHoF ₄ from Bitko et al. [1]	9
2.3	Full $B_x - T$ phase diagram of LiHoF ₄	13
2.4	Schematic illustration of induced transverse local fields	15
2.5	Energy vs. B_x of the single Ho electronic states	16
3.1	Energy and magnetic moment vs. B_z	19
3.2	Example of equilibration process	26
3.3	Example of binning analysis	28
4.1	ζ_L/L vs. T for $B_x = 0.0$ with ODD terms	32
4.2	ζ_L/L vs. T for $B_x = 0.0$ without ODD terms	33
4.3	ζ_L/L vs. T for $B_x = 0.3$ T with ODD terms	33
4.4	ζ_L/L vs. T for $B_x = 0.3$ T without ODD terms	34
4.5	Phase diagram of LiHoF ₄ with numerical results	35
4.6	Standard deviation of local B_x vs. T	37
A.1	Energy levels vs. the expected value of J_z	43
B.1	Convergence tests of the Ewald sums	46

List of Tables

D.1	Summary of simulation results	50
D.2	Simulation parameters for $L = 4$, $B_x = 0.0$, without ODD terms	51
D.3	Simulation parameters for $L = 5$, $B_x = 0.0$, without ODD terms	52
D.4	Simulation parameters for $L = 6$, $B_x = 0.0$, without ODD terms	53
D.5	Simulation parameters for $L = 4$, $B_x = 0.3$, without ODD terms	54
D.6	Simulation parameters for $L = 5$, $B_x = 0.3$, without ODD terms	55
D.7	Simulation parameters for $L = 6$, $B_x = 0.3$, without ODD terms	56
D.8	Simulation parameters for $L = 4$, $B_x = 0.0$, with ODD terms	57
D.9	Simulation parameters for $L = 5$, $B_x = 0.0$, with ODD terms	58
D.10	Simulation parameters for $L = 6$, $B_x = 0.0$, with ODD terms	59
D.11	Simulation parameters for $L = 4$, $B_x = 0.3$, with ODD terms	60
D.12	Simulation parameters for $L = 5$, $B_x = 0.3$, with ODD terms	61
D.13	Simulation parameters for $L = 6$, $B_x = 0.3$, with ODD terms	62

1 Introduction

1.1 LiHoF₄

LiHoF₄ is a rare-earth compound in which only the Holmium ions, Ho^{3+} , are magnetic. The predominant interactions between the Ho^{3+} ions in LiHoF₄ are long-range dipolar interactions. The Ho^{3+} ions are also subjected to a highly anisotropic crystal field potential which splits its 17-fold degenerate ground state, leaving a ground state doublet and a first excited state at $\sim \Omega_0 = 11$ K above it [7] (see also appendix A.2). This means that at temperature $T \ll \Omega_0$ LiHoF₄ is a good realization of the Ising model with dipolar interactions. Quantum fluctuations between the two Ising states can be induced by a transverse magnetic field, B_x , making it such that LiHoF₄ is well described by the transverse field Ising model (TFIM) [3]. Disorder can be added to the system by dilution of Ho with Y to get LiHo_xY_{1-x}F₄. Since Y and Ho ions have very similar volumes and Y ions are non-magnetic, the dilution adds randomness to the magnetic interaction without significantly affecting the lattice structure [8, 9]. It has been established that in the diluted case, interplay between the off-diagonal dipolar interaction and the transverse magnetic field gives rise to effective longitudinal random fields [10–12]. Experimentally, at high temperatures LiHoF₄ is a paramagnet (PM), with a phase transition to a ferromagnetic (FM) state occurring at $T_c = 1.53$ K. This critical temperature can be lowered by applying an external magnetic field transverse to the magnetic easy-axis of the crystal, which renormalizes the magnetic moments and induces fluctuations between the two Ising ground states. At a critical value of $B_c \approx 4.9$ T a zero-temperature transition occurs between a ferromagnetic and paramagnetic phase [1].

Several works attempted to formulate a theoretical description of LiHoF₄, either by establishing a correspondence with the TFIM and deriving the effective parameters [3] or by mean-field solutions to the full microscopic

Hamiltonian [4, 5]. All of these attempts seem to estimate a critical temperature that is higher than the well established experimental result at zero transverse field. The nearest neighbor exchange interaction strength, J_{ex} , has been used as a fitting parameter in many of these works, as there has been no direct determination of its magnitude. Being antiferromagnetic in nature, the exchange interaction acts to lower the critical temperature, and thus J_{ex} was used to tune the expected T_c value to be in agreement with the experimental value. Even though the T_c value at zero applied transverse field, $T_c(0)$, could be tuned in such a way to match experimental results, there still remains a significant discrepancy between the theoretical predictions and the experimental data. Specifically, near $T_c(0)$ the phase boundary rises much more steeply than predicted by the model, as can be seen in figure 1.1 – that is it has a much weaker dependence on the applied field than expected.

Subsequent numerical works were made in an attempt to improve upon these results, both by employing alternative numerical methods and by using different sets of crystal-field parameters, but were ultimately unsuccessful in explaining the discrepancy [2]. Additional experimental works were also performed in the time since the original determination of the phase diagram by Bitko et al. [1], using various other methods, but they mostly agree with those original experiments and even accentuate the discrepancy in the low B_x region [5, 6]. Thus, the steep rise of the phase boundary near T_c remains an open question [9].

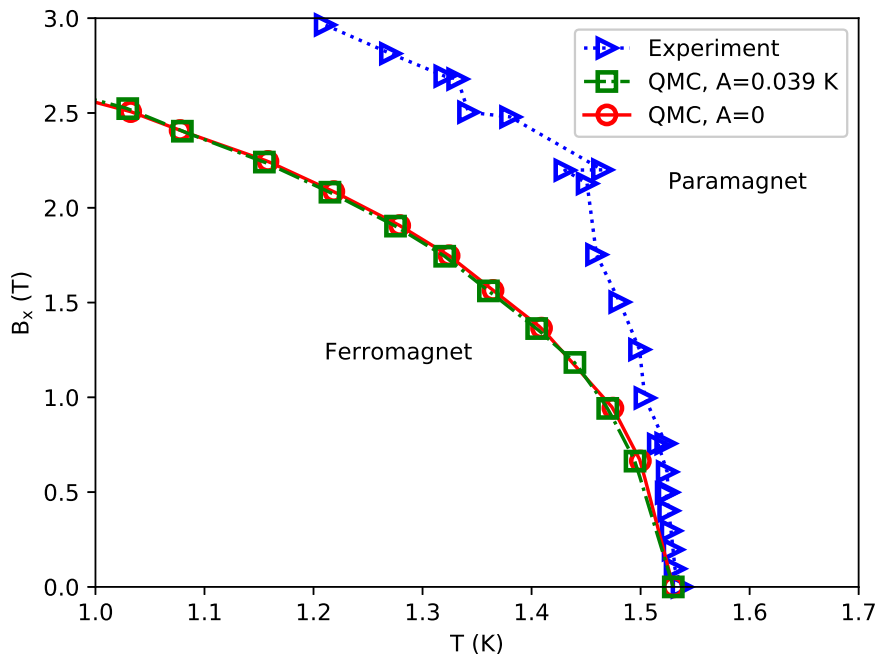


Figure 1.1: Low B_x phase diagram of LiHoF_4 . The discrepancy between experimental data compiled in ref. [5] and QMC simulations from ref. [3] can be seen in this region. Other attempts at deriving the phase diagram using different Monte Carlo simulations and different sets of crystal-field parameters can be seen in ref. [2] to have the same discrepancy.

1.2 Transverse Field Ising Model

As mentioned, LiHoF_4 in an external transverse magnetic field is a good realization of the transverse field Ising model (TFIM) [1]. The Hamiltonian of the TFIM is given by

$$H_{\text{TFIM}} = -\frac{1}{2} \sum_{ij} J_{ij} S_i^z S_j^z - \Gamma \sum_i S_i^x \quad (1.1)$$

where $S^z \equiv \frac{1}{2}\sigma^z$, $S^x \equiv \frac{1}{2}\sigma^x$ are spin- $\frac{1}{2}$ operators and the i, j subscripts indicate the site on which they act. Here σ^z, σ^x are the familiar Pauli matrices. The eigenstates of the S^z operator are denoted by $|\uparrow\rangle$ and $|\downarrow\rangle$ and have

eigenvalues $+\frac{1}{2}$ and $-\frac{1}{2}$ respectively. When $\Gamma = 0$, H_{TFIM} is diagonal in the basis of eigenstates of S_i^z , which makes it the simple classical Ising model. With $\Gamma \neq 0$, the S_i^x term causes tunneling between the *up* and *down* eigenstates of S^z that flips the orientation of the Ising spin at site i and decrease the critical temperature T_c at which the system exhibits long range order. For the simplest case of fixed ferromagnetic interaction, $J_{ij} = J > 0$, between nearest neighbors, the mean-field solution is given by the relation [1]

$$\coth\left(\frac{\Gamma}{k_B T_c}\right) = \frac{J}{\Gamma} \quad (1.2)$$

which is schematically plotted in figure 1.2. There one can see the resemblance to the full phase diagram of LiHoF_4 plotted in figure 2.2.

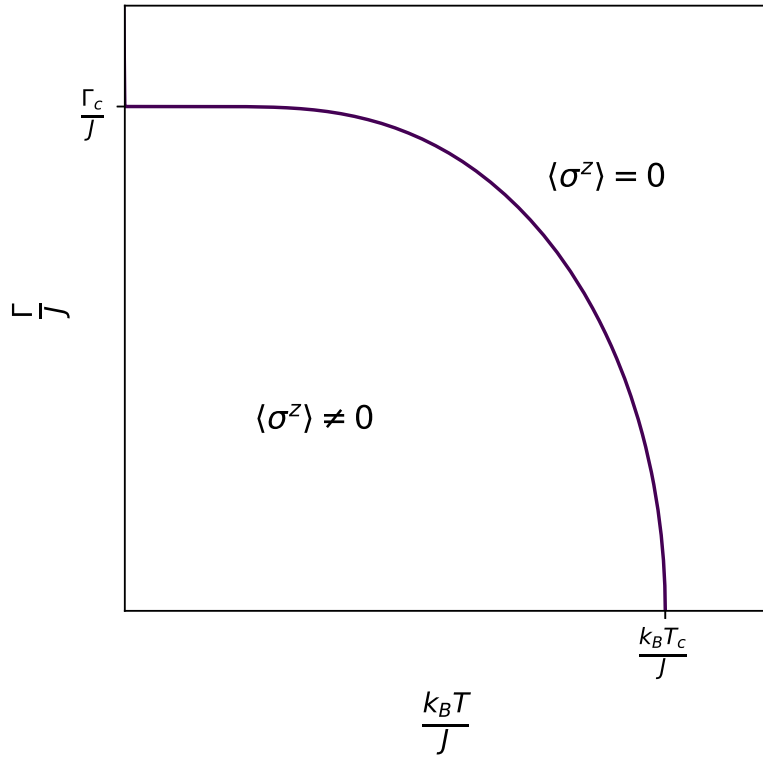


Figure 1.2: Mean field phase diagram of TFIM

1.3 Outline

Chapter 2 starts with a basic description of the LiHoF_4 crystal and the single Ho ion electronic states which provide the theoretical justification for its treatment as a TFIM-like system. Next, two classes of previous theoretical attempts at describing the phase diagram of LiHoF_4 as presented. The first is mean-field calculations by Bitko et al. [1] and some subsequent works [4, 5], and the second is a derivation of an effective spin- $\frac{1}{2}$ Hamiltonian describing the low-energy behavior of the system and performing Monte Carlo simulations to get the phase diagram from it [2, 3]. In section 2.5 we explain the importance of offdiagonal dipolar (ODD) terms to the phase diagram and how they might explain the discrepancy between experimental results and previous attempts at a theoretical description. We then present the Hamiltonian that will be investigated numerically in this work.

In chapter 3 we present the numerical methods used in this work, including Monte Carlo simulations and the various methods used to find self-consistent states during those simulations. Later, the methods used to analyze the results of said simulations and establish their validity are explained. The results are presented in chapter 4, where the effect of inclusion vs. exclusion of the ODD terms is discussed. There we make the case that their inclusion is necessary to appropriately describe the phase diagram, and that it could help explain the previously detailed discrepancy. A summary of the results and analysis is given in chapter 5.

Appendix A.1 has a detailed discussion of the single-ion electronic states that are the basis of every theoretical treatment of LiHoF_4 . Appendix A.2 features a derivation of the crystal field potential applied to the Ho ions, and details the crystal-field parameters used in this work. Appendix B explains the Ewald summation method that was used to deal with the long-range dipolar interaction with periodic boundary conditions. It also includes the numerical parameters chosen for the method and shows the convergence of the results. Appendix C consists of the technical details of the interpolation procedure that is used to obtain approximations of quantities required for the simulation. Lastly, parameters of the simulations and numerical results are given in appendix D.

2 Theory

2.1 Crystal Structure and Microscopic Hamiltonian of LiHoF₄

LiHoF₄ forms a tetragonal structure with lattice constants $a = 5.175 \text{ \AA}$ and $c = 10.75 \text{ \AA}$. There are four Ho^{3+} ions per unit cell which form a lattice with a basis with coordinates $(0, 0, \frac{1}{2})$, $(0, \frac{1}{2}, \frac{3}{4})$, $(\frac{1}{2}, \frac{1}{2}, 0)$ and $(\frac{1}{2}, 0, \frac{1}{4})$ [9], as can be seen in Figure 2.1. The crystal has S_4 symmetry which will enable us to express its crystal-field potential, V_C , in terms of angular momentum operators of the Ho^{3+} ions (see appendix A.2). The complete Hamiltonian of LiHoF₄ in a transverse magnetic field is given by [3]

$$H = \sum_i V_C(\mathbf{J}_i) - g_L \mu_B \sum_i B_x J_i^x + \frac{1}{2} (g_L \mu_B)^2 \sum_{i \neq j} V_{ij}^{\mu\nu} J_i^\mu J_j^\nu + J_{\text{ex}} \sum_{\langle i,j \rangle} \mathbf{J}_i \cdot \mathbf{J}_j + A \sum_i (\mathbf{I}_i \cdot \mathbf{J}_i) \quad (2.1)$$

where $V_{ij}^{\mu\nu}$ is the magnetic dipole interaction,

$$V_{ij}^{\mu\nu} = \frac{\delta^{\mu\nu} |\vec{r}_{ij}|^2 - 3(\vec{r}_{ij})^\mu (\vec{r}_{ij})^\nu}{|\vec{r}_{ij}|^5}. \quad (2.2)$$

J_{ex} is the nearest-neighbor exchange interaction coupling constant. $\mu_B = 0.6717 \text{ K T}^{-1}$ is the Bohr magneton and $g_L = \frac{5}{4}$ is a Landé g-factor. \mathbf{J}_i are angular momentum operators of the Ho^{3+} ions. A is the hyperfine interaction strength, and \mathbf{I}_i is the nuclear spin operator, where the total Ho nuclear spin is $I = \frac{7}{2}$.

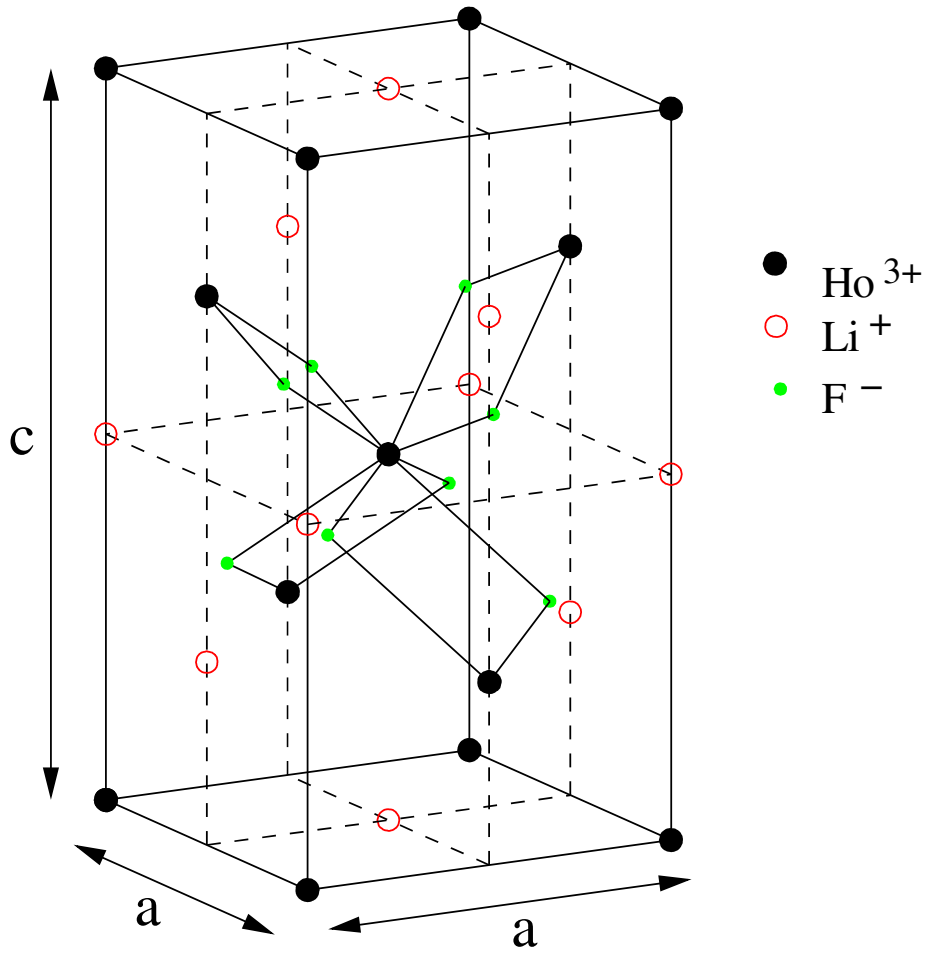


Figure 2.1: Unit cell structure of LiHoF_4 . The direction along the c axis is the Ising axis and the external magnetic field B_x is applied perpendicular to that axis in experiments. Figure taken from Gingras and Henelius [9].

2.2 Mean-Field Solution

An early attempt to determine the $B_x - T$ phase diagram of LiHoF_4 via susceptibility measurements was done by Bitko et al. [1], where they also fit their experimental data to the full mean-field Hamiltonian of a single Ho^{3+} ion. The procedure they employed used the Hamiltonian

$$H_{\text{mean-field}} = V_C - g_{\perp} \mu_B B_x \hat{J}_x + A(\hat{I} \cdot \hat{J}) - 2J_0 \langle \hat{J}_z \rangle \hat{J}_z \quad (2.3)$$

which was solved self-consistently. Here $J = 8$, $I = \frac{7}{2}$, V_C is the crystal-field potential, g_{\perp} is the transverse g -factor, A is the hyperfine coupling constant, and J_0 is an average spin-spin longitudinal coupling strength. g_{\perp} and J_0 were fitted to match the experimental results, giving $J_0 = 0.0270 \pm 0.0005 \text{ K}$ and $g_{\perp} = 0.74 \pm 0.04$. This 136×136 Hamiltonian was used to find T_c as a function of B_x by fixing B_x and calculating $\langle \hat{J}_z \rangle$ self-consistently starting from a high temperature and decreasing it until a non-zero magnetization is numerically observed. This procedure gives the solid line in figure 2.2. Next, the same procedure is repeated with the best-fit values found previously, but without the hyperfine interaction, so that (2.3) becomes a 17×17 matrix. The resulting phase boundary is plotted in figure 2.2 as a dashed line. For the low- B_x regime we see that the inclusion of the hyperfine interaction has no noticeable influence on the phase diagram, indicating that the splitting due to the hyperfine interaction is small compared to $T_c(B_x \approx 0)$ and may be neglected in this range. The mean-field treatment is lacking in two respects. First it introduces a phenomenological effective g -factor for the transverse field, and second, though it matches the experimental critical temperature $T_c(B_x = 0)$ and critical transverse field $B_x^c(T = 0)$, it is not as good in the intermediate B_x regime. Further experiments show that there is indeed a real, persistent discrepancy in the low- B_x regime [5, 6].

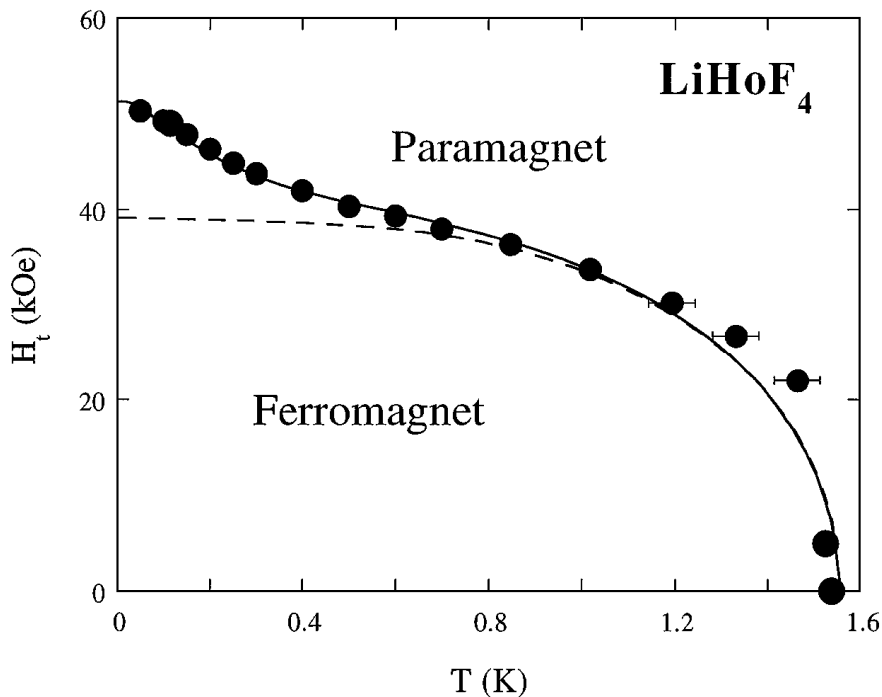


Figure 2.2: $B_x - T_c$ phase diagram of LiHoF₄ from Bitko et al. [1]. Experimental phase boundary (full circles) for the ferromagnetic transition. Dashed line is a mean-field solution without the hyperfine interaction and solid line is the full mean-field fitted solution.

Subsequent work by Rønnow et al. [4] sought to address these issues. First, Rønnow et al. presented a new set of crystal-field parameters (CFPs, see appendix A.2) that in addition to susceptibility measurements [13] also incorporate results from several spectroscopic investigations (listed in ref. [4]). This set of CFPs, listed in (A.6), is the one used in this work as well. With this new set of CFPs, the only free parameter in the microscopic Hamiltonian (2.1) is the nearest-neighbor exchange interaction J_{ex} [4]. Rønnow et al. used this new set of CFPs to reproduce the mean-field model, and found that the fit that agrees with the low-temperature experimental results predicts $T_c(0)$ between 1.8 and 1.85 K instead of the known 1.53 K. Therefore they conclude that fluctuations must be taken into account, which they do by using the so called *effective-medium theory* to first order in the $1/z$ expansion [4]. Additionally, they perform inelas-

tic neutron scattering tests and try to fit the theoretical $1/z$ results to the experimental ones by Bitko et al. and their own. They find that the $1/z$ expansion gives $T_c(0) = 1.74\text{K}$ which is closer to the experimental value than the simple mean-field result, but still not in agreement with it.

Different choices of J_{ex} can mitigate the discrepancy at low B_x at the cost of differing significantly from experimental results in the intermediate regime of $2\text{T} < B_x < 4\text{T}$, as can be seen with the dotted line in figure 2.3. Hence one might conclude that mean-field like models might be missing some essential element of the physics around the classical transition, and therefore J_{ex} should be chosen to match the high- B_x regime, as with the solid blue line in figure 2.3.

2.3 Effective Spin- $\frac{1}{2}$ Hamiltonian for LiHoF₄

A second approach to investigating the phase diagram is to start from the full microscopic Hamiltonian of the LiHoF₄ crystal in a transverse magnetic field given by eq. (2.1), and recast it as an effective spin- $\frac{1}{2}$ Ising model with an effective transverse field. Most of the previous work in this direction was done by Chakraborty et al. [3] who established a correspondence between the full microscopic Hamiltonian and the TFIM and then performed quantum Monte Carlo (QMC) simulations to obtain the phase diagram. We briefly review that derivation before we can discuss its possible shortcomings that may lead to the discrepancy described in chapter 1. The basis for the derivation comes from the fact that diagonalizing the crystal field Hamiltonian V_C gives a ground state doublet with the next lowest excited state about 11 K above it. At temperatures around $T_c \sim 1.5\text{K}$ we can expect only the ground state doublet to be significantly occupied, which creates an effective two-state Ising system. Denoting the degenerate ground states by $|\alpha\rangle$ and $|\beta\rangle$, they can be chosen such that $\langle\alpha|J^z|\alpha\rangle = -\langle\beta|J^z|\beta\rangle$ and $\langle\alpha|J^z|\beta\rangle = 0$. Then we find that the operators J_x, J_y have no nonzero matrix elements between the states $|\alpha\rangle$ and $|\beta\rangle$. This will be a key point in explaining our hypothesis later. For now, the degenerate ground states, chosen as described, can be identified as the $|\uparrow\rangle$ and $|\downarrow\rangle$ states of the effective Ising model. To account for the role of the external transverse field, Chakraborty et al. [3] diagonalize the single-site Hamiltonian which includes the crystal field potential and the Zeeman term of the external magnetic field,

$$H_{\text{single-site}} = V_C - g_L\mu_B B_x J^x \quad (2.4)$$

For a given value of B_x , the two lowest lying states are denoted by $|\alpha(B_x)\rangle$ and $|\beta(B_x)\rangle$, and their energies by $E_\alpha(B_x)$ and $E_\beta(B_x)$ respectively. The two states remain at least 10 K below the next excited level, so that we still treat the two-dimensional space spanned by these states as our Ising space. The basis of the subspace is chosen by unitary rotation of the states $|\alpha(B_x)\rangle$ and $|\beta(B_x)\rangle$ according to (the B_x dependence is dropped for brevity)

$$\begin{aligned} |\uparrow\rangle &= \frac{1}{\sqrt{2}} [|\alpha\rangle + \exp(i\theta) |\beta\rangle] \\ |\downarrow\rangle &= \frac{1}{\sqrt{2}} [|\alpha\rangle - \exp(i\theta) |\beta\rangle] \end{aligned} \quad (2.5)$$

where the angle θ is chosen so that the matrix elements of J^z between the states $|\uparrow\rangle$ and $|\downarrow\rangle$ are real and diagonal. Such a choice means that J^z , projected onto the low-energy subspace, is represented by $C_{zz}\sigma^z$ where C_{zz} is a constant of proportionality. The other angular momentum operators are similarly projected onto the Ising subspace. Practically this amounts to numerically finding the parameters $C_{\mu\nu}$ in

$$J^\mu = C_\mu + \sum_{\nu=x,y,z} C_{\mu\nu}(B_x)\sigma^\nu. \quad (2.6)$$

Once the coefficients are found, the J operators are replaced by their two-dimensional projections in the full Hamiltonian (2.1), which results in many interaction terms between the effective Ising spins. Among these interactions, the largest effective interaction is found to be $J_i^z J_j^z \propto (C_{zz})^2 \sigma_i^z \sigma_j^z$ which is larger by two orders of magnitude than any other term except for some constants that may be discarded by recalibrating the energy scale [3]. Therefore, an effective Hamiltonian is introduced,

$$\begin{aligned} H_{\text{Ising}} = -\frac{\Delta(B_x)}{2} \sum_i \sigma_i^x + \frac{1}{2} (g_L \mu_B C_{zz}(B_x))^2 \sum_{i \neq j} V_{ij}^{zz} \sigma_i^z \sigma_j^z + \\ J_{\text{ex}} (C_{zz}(B_x))^2 \sum_{\langle i,j \rangle} \sigma_i^z \sigma_j^z. \end{aligned} \quad (2.7)$$

This Hamiltonian is then used to obtain the phase diagram in figure 1.1 using QMC. The resulting critical temperature is found to be $T_c(0) = 2.03$ K which is significantly higher than the experimental value. Using the free parameter J_{ex} , the critical temperature is tuned to match the experimental value of 1.53 K, though the predicted $T_c(B_x)$ dependence for $B_x > 0$ is still inconsistent with experiment.

The discrepancy with the data close to the zero-field transition was attributed by the authors to uncertainties in the crystal-field parameters. The same Hamiltonian (2.7) was further investigated by Tabei et al. [2] with the goal of examining various effects that may be the source of this discrepancy. Particularly, they perform classical Monte Carlo in which quantum effects are incorporated perturbatively, using different sets of CFPs, and handling the long-range dipole-dipole interactions in different ways. None of these variations is found to significantly change the resulting phase diagram and bring it to closer agreement with experiments. Hence we conclude that the discrepancy is neither of computational origin, nor is it a consequence of uncertainties in CFPs.

2.4 Nearest-Neighbor Exchange Interactions

An important factor that has significant influence on the phase diagram is the nearest-neighbor exchange interaction, J_{ex} . The exchange interaction is antiferromagnetic in nature, so that it favors anti-aligned spins, which means that its main effect is to suppress the critical temperature. The exchange interaction is considered to be weak compared to the dipolar interaction [3] based on the limited spatial extent of the unfilled $4f$ electronic orbitals of the Ho^{3+} ions [9], but it has not been measured directly [3]. Therefore, it is used in many of the theoretical models as a fitting parameter used to generate the correct zero-field transition temperature. We specifically mention two possible values for J_{ex} . First, the one found in Monte Carlo simulations [14] of $J_{\text{ex}} = 3.95$ mK which is in close agreement with the value of $J_{\text{ex}} = 3.91$ mK determined by Tabei et al. [2]. The second value is $J_{\text{ex}} = 1.16$ mK which was found by Rønnow et al. [4] by fitting to inelastic neutron scattering measurements such that good agreement is obtained when $2\text{T} < B_x < 4\text{T}$. This value overestimates the zero-field critical temperature in their calculations by 14 percent compared with the experimental zero-field critical temperature as can be seen in figure 2.3.

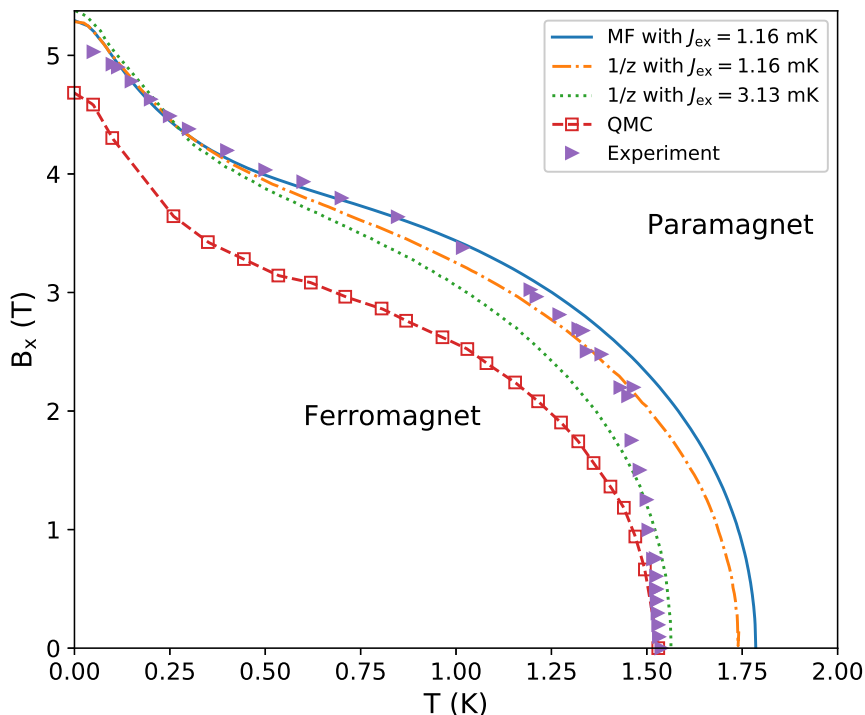


Figure 2.3: Full phase diagram of LiHoF₄ as a function of temperature and applied transverse field. Open squares are quantum Monte Carlo (QMC) results from ref. [3]. The dotted line is the $1/z$ calculation with $J_{\text{ex}} = 3.13$ mK and the dot-dashed line is the same calculation with $J_{\text{ex}} = 1.16$ mK, both from ref. [4]. The solid line is a mean-field (MF) calculation taken from ref. [5]. Triangles represent results of several different experiments [1, 5, 6] compiled in ref. [5]. An apparent trade off is observed between theoretical predictions that match the experimental results at low temperatures but completely fail at the low-field regime, and ones that give the correct zero-field T_c but fail to predict the correct $T_c(B_x)$ dependence and give a poor match at the intermediate B_x region.

2.5 Proposed Hamiltonian

As mentioned in section 2.3, with $B_x = 0$ the only terms that remain in the effective Hamiltonian are those representing zz interactions. This statement is exact within the framework used by Chakraborty et al. [3], wherein the angular momentum operators are projected onto the low-energy two-dimensional subspace. This is a direct result of the fact that the J^x, J^y operators have no nonzero matrix elements between the states $|\uparrow\rangle$ and $|\downarrow\rangle$.

Still, J^x and J^y do couple the two Ising states in second order in the transverse magnetic field, and even more importantly, second order corrections to the expectation values $\langle\uparrow|J^z|\uparrow\rangle$, $\langle\downarrow|J^z|\downarrow\rangle$ and the corresponding energies are expected through mixing with higher levels. This second order effect is effectively neglected by the direct projection of the operators.

Offdiagonal terms of the dipolar interaction have been known to give rise to many interesting phenomena in the diluted case of $\text{LiHo}_x\text{Y}_{1-x}\text{F}_4$ [8, 10–12, 15, 16] where they obviously do not cancel by symmetry. We argue that similar effects, arising from internal transverse fields exerted by the $\langle J_i^z \rangle$ expectation values on the x angular momentum component J_j^x through terms of the form $V_{ij}^{zx} \langle J_i^z \rangle J_j^x$, make a significant impact on the phase diagram even in the undiluted case. The reason is captured by the following heuristic argument. First we consider some specific spin. In the ferromagnetic phase, with infinite correlation length, any pair of mirror spins will be correlated so that the effective transverse field they exert on the spin of focus is canceled by symmetry. In contrast, in the paramagnetic phase, assuming vanishing correlation length, any two such spins will be uncorrelated, so that the fields they exert may either cancel or add together with equal probability. The resulting thermal averaged field is obviously zero, but a non-zero variance of that field is expected. See illustration in figure 2.4.

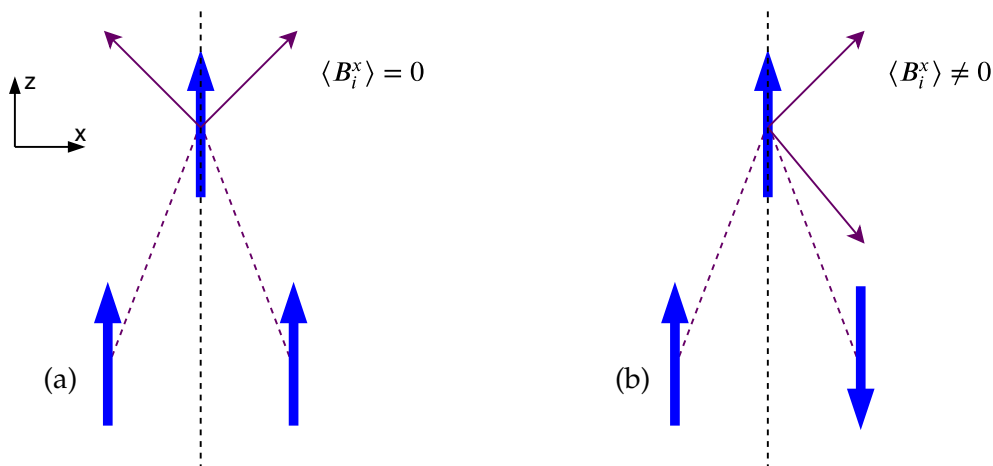


Figure 2.4: Schematic illustration of the induction of transverse local fields in the paramagnetic phase. The two spins at the bottom are located symmetrically with respect to the plane that includes the upper spin and is parallel to the $y - z$ plane. (a) In the ferromagnetic phase the two spins at the bottom are correlated so that the fields they induce on the third spin cancel out by symmetry. (b) In the paramagnetic phase the two spins at the bottom are uncorrelated and may induce a nonzero transverse magnetic field on the third spin.

Considering a single Ho ion subject to a transverse magnetic field and under the crystal-field potential, we see that the energy of both the lowest laying energy states is reduced as the transverse field is increased, as can be seen in figure 2.5. This means that the typical magnitudes of the local transverse fields control the energy of the system, i.e. the system can lower its energy by choosing configurations that induce larger transverse fields. Another important effect of the transverse fields is to decrease the absolute value of $\langle J^z \rangle$ for both of the lowest energy states, by mixing them with the higher electronic states. This also lowers the total energy of the system just by reducing the dominant zz dipolar term proportional to $\langle J^z \rangle^2$.

Hence, these offdiagonal dipolar terms lower the energy of the paramagnetic phase compared to that of the ferromagnetic phase, and should thus decrease the critical temperature. This effect, by its nature, is not likely to be captured in any sort of mean-field like analysis as it depends on the spatial fluctuations of the states. We posit that including these terms is necessary to explain the previously mentioned discrepancy between theory and experiment. We wish to build upon the previous results by Chakraborty

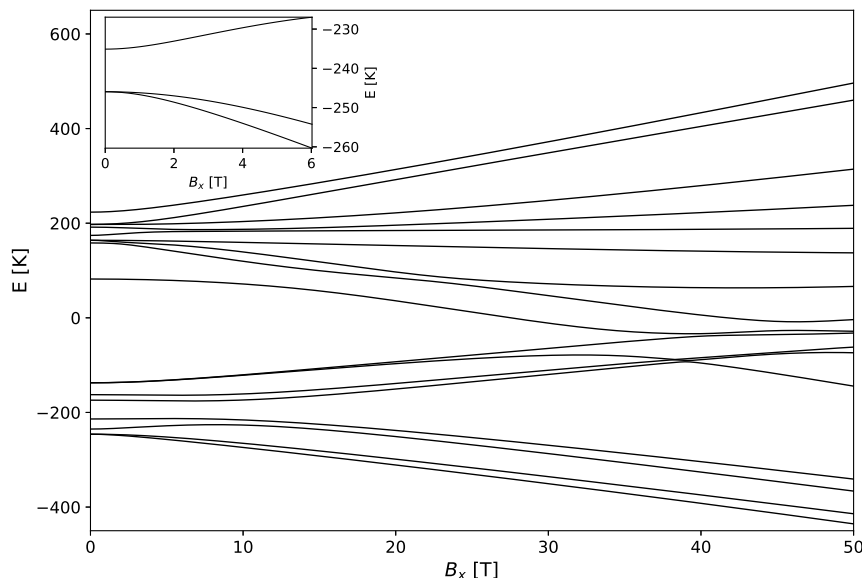


Figure 2.5: Energy vs. B_x of the single Ho electronic states. Energy of the 17 electronic states of a single Ho ion, under crystal field potential, as a function of transverse magnetic field B_x . The two lowest laying states can be seen to decrease monotonically with B_x . The inset shows the three lowest energy levels in the range $0 < B_x < 6$ T. The gap between the two lowest energy levels and the next excited level can be seen to only increase with B_x .

et al. [3] described in 2.3 but add the internal transverse magnetic fields that have been effectively neglected thus far. With that in mind, we return to the full microscopic Hamiltonian of (2.1). Of the diagonal dipolar terms, we keep only the zz interactions which have been established as the most dominant, but we also keep the offdiagonal interaction terms. The dipolar interaction, given in (2.2), is invariant under both $i \leftrightarrow j$ and $\mu \leftrightarrow \nu$. We also use the fact that $[J_i^x, J_j^z] = 0$ and $[J_i^y, J_j^z] = 0$ when $i \neq j$. In accordance with previous results we also keep only the zz term among the three exchange interaction terms. Additionally, we neglect the hyperfine interaction altogether, as it was found not to cause a significant difference in this section of the $B_x - T$ phase diagram. We rearrange the remaining

terms of the Hamiltonian to get

$$H_{\text{eff}} = \sum_i V_C(J_i) - g_L \mu_B \sum_i B_x J_i^x + \frac{1}{2} (g_L \mu_B)^2 \sum_{i \neq j} V_{ij}^{zz} J_i^z J_j^z + (g_L \mu_B)^2 \sum_{i \neq j} V_{ij}^{zx} J_j^z J_i^x + (g_L \mu_B)^2 \sum_{i \neq j} V_{ij}^{zy} J_j^z J_i^y + J_{\text{ex}} \sum_{\langle i,j \rangle} J_i^z J_j^z \quad (2.8)$$

Then, we group together the terms which constitute effective internal magnetic fields so that

$$H_{\text{eff}} = \sum_i V_C(J_i) - g_L \mu_B \sum_i \mathbf{B}_i \cdot \mathbf{J}_i + J_{\text{ex}} \sum_{\langle i,j \rangle} J_i^z J_j^z \quad (2.9)$$

where

$$\begin{aligned} B_i^x &= B_x - g_L \mu_B \sum_{j \neq i} V_{ij}^{zx} J_j^z \\ B_i^y &= -g_L \mu_B \sum_{j \neq i} V_{ij}^{zy} J_j^z \\ B_i^z &= -\frac{1}{2} g_L \mu_B \sum_{j \neq i} V_{ij}^{zz} J_j^z \end{aligned} \quad (2.10)$$

are the effective internal fields. The Monte Carlo simulation procedure requires that we switch between the many-body states of the system, calculating their energy and measuring the observables of interest. The single-site Hamiltonian, given by the first two terms in (2.9), is solved self-consistently for the expectation values $\{\langle J_i^z \rangle\}$ as in

$$H_{\text{eff}} = \sum_i V_C(\vec{J}_i) - g_L \mu_B \sum_i \langle \mathbf{B}_i \rangle_\psi \cdot \mathbf{J}_i + J_{\text{ex}} \sum_{\langle i,j \rangle} J_i^z J_j^z. \quad (2.11)$$

Thus we construct many-body states for the simulation by diagonalizing the single-site Hamiltonian, choosing one of its eigenstates and taking the product of all these states as a many-body state. The expectation values are determined self consistently in a procedure described in section 3.2 such that the single-site states that determine the expectation values of the fields are compatible with those fields. In other words, we neglect quantum many-body effects such as entanglement and instead consider each ion separately. Nevertheless, the single ion is treated exactly by diagonalization of its Hamiltonian in a manner that is self-consistent with all other ions. Periodic boundary conditions are used, and the dipolar interaction (2.2) is calculated using the Ewald summation method described in appendix B.

3 Numerical Methods

3.1 Diagonalization of the single-site Hamiltonian

The framework used in this work requires that each Ho site have two states, designated *up* and *down*, and that each of these states have its own energy and magnetic moment that are functions of the local magnetic field. The determination of these two quantities requires diagonalizing the single-site Hamiltonian,

$$H_{\text{single-site}} = V_C(\mathbf{J}) - g_L \mu_B \mathbf{B} \cdot \mathbf{J}. \quad (3.1)$$

We diagonalize this Hamiltonian numerically and designate its two low energy levels $|\alpha\rangle$ and $|\beta\rangle$ such that $E_\alpha < E_\beta$. The case of degeneracy arises only for $B_z = 0$ which we exclude assuming within the simulation the local B_z will always some nonzero value. Next, the states $|\alpha\rangle$ and $|\beta\rangle$ are identified as $|\uparrow\rangle$ or $|\downarrow\rangle$ according to their $\langle J^z \rangle$ in the following manner: If $\langle \alpha | J^z | \alpha \rangle > \langle \beta | J^z | \beta \rangle$ then $|\alpha\rangle \equiv |\uparrow\rangle$ and $|\beta\rangle \equiv |\downarrow\rangle$ and vice versa otherwise. In the range of \mathbf{B} discussed in this work this is a one-to-one relation, except for the mentioned $B_z = 0$ case. The two required quantities, energy and magnetic moment, are calculated in this process, and are used throughout the simulation.

The process of exact diagonalization described above is quite computationally intensive and performing it multiple times for each spin-flip, as required for the self consistent calculation (see section 3.2), is not feasible. The solution that was chosen to address this difficulty is to obtain the required quantities approximately by calculating them ahead of time on a grid of B_x , B_y and B_z and saving the results. Then, during the simulation a linear interpolation scheme is used to approximate these quantities for arbitrary \mathbf{B} , using the pre-calculated values. The interpolation scheme works as follows: For a single site with given (B_x, B_y, B_z) , first the clos-

est values in each dimension are located in the interpolation table. The procedure is made more efficient by exploiting the fact that for each spin, subsequent searches are highly correlated, as they occur following each spin-flip, and the local fields are not expected to change significantly. The exact algorithm for finding the closest values is detailed in ref. [17, subsection 3.1.1]. Once the two closest values in each direction are found, the value is calculated by trilinear interpolation, the details of which are given in appendix C.

This scheme gives rise to two issues worth noting, the density of pre-calculated points, and the minimum and maximum pre-calculated values. Both are chosen with the assumption (which is self-consistently confirmed later) that the typical fields encountered during the simulation are not very large, and therefore we choose the values so that they are more dense around $\mathbf{B} = 0$ and the maximum and minimum to be $\sim \pm 2$ T. In the (rare) case when the local magnetic field falls outside the bounds of the table, the required values are calculated directly, by exact diagonalization of the Hamiltonian in (3.1). The density of the table can have a significant effect around $B_z = 0$, that will be discussed in section 4.1. Figure 3.1 shows a slice of the interpolated functions with exact values for comparison. The largest difference between the two for $\langle J^z \rangle$ is around $B_z = 0$.

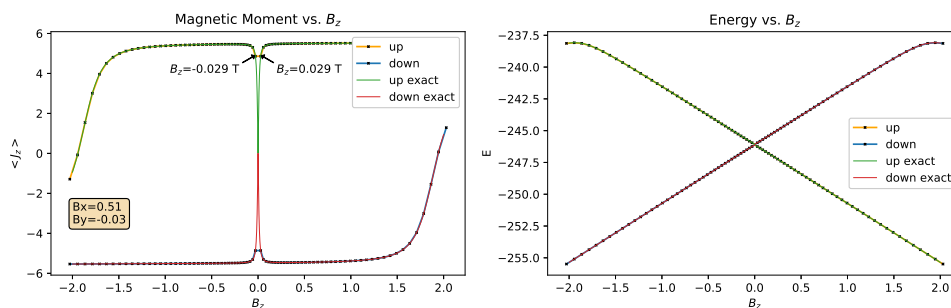


Figure 3.1: Energy and magnetic moment vs. B_z . On the left is the magnetic moment $\langle J^z \rangle$ plotted against B_z for $B_x = 0.51$ T and $B_y = -0.03$ T. On the right is the energy against B_z for the same parameter values. Both graphs show the pre-calculated values as small black Xs and the linear interpolation between them. Additionally the exact values are plotted in red and green. The largest difference between the two is easily observed for the magnetic moments between the two points explicitly denoted on the graph, $B_z = \pm 0.029$ T.

3.2 Self-consistent calculation

Our procedure requires that we find valid states of the full system. We construct such states from the Hamiltonian in (2.11) by finding single-site states that are eigenstates of the first two terms of eq. (2.11). Each site is designated "up" or "down" within the Monte Carlo scheme, so that one of the low energy states is chosen according to this designation and the J^z expectation value as described in section 3.1. Then the full state of the system is taken as the product of all the single-site states. This enables us to recalculate the value of $\langle \mathbf{B}_i \rangle_\psi$ with the newly obtained ψ (as described in section 3.1), which in turn modifies the single-site states and thus their J^z expected values. We wish to find states ψ that self-consistently satisfy both conditions, i.e. being a product of eigenstates of the single-site Hamiltonian with given $\langle \mathbf{B}_i \rangle_\psi$, and indeed inducing those $\langle \mathbf{B}_i \rangle_\psi$. In order to get such states we use one of two numerical methods which will be described in the remainder of this section. First we redefine the problem in more general terms. The full states are not actually required for the Monte Carlo process, but only the $\langle J_i^z \rangle$ values for each of the sites, from which we can calculate the energy of the state and all observables of interest for the purpose of finding the phase transition. Hence, we actually need to find the roots of a nonlinear system of equations,

$$\begin{aligned} f_1(x_1, \dots, x_N) &= 0 \\ &\vdots \\ f_N(x_1, \dots, x_N) &= 0 \end{aligned} \tag{3.2}$$

where $f_i(x_1, \dots, x_N)$ is one of two functions,

$$f_i(x_1, \dots, x_N) = \begin{cases} g_{i\uparrow}(x_1, \dots, x_N) - x_i & \text{or} \\ g_{i\downarrow}(x_1, \dots, x_N) - x_i \end{cases} \tag{3.3}$$

and

$$g_{i\chi_i}(x_1, \dots, x_N) = \langle \chi_i(\mathbf{B}_i(x_1, \dots, x_N)) | J_i^z | \chi_i(\mathbf{B}_i(x_1, \dots, x_N)) \rangle \tag{3.4}$$

depending on the current thermal configuration of the system within the Monte Carlo procedure with $\chi_i \in \{\uparrow, \downarrow\}$. The variables x_1, \dots, x_N are the expectation values $\langle J_1^z \rangle, \dots, \langle J_N^z \rangle$. In practice the expectation values in $f_i(x_1, \dots, x_N)$ are approximated by trilinear interpolation as explained in section 3.1.

One important note is that within this framework the orientations of the spins are set by the Monte Carlo simulation. The self-consistent calculation cannot change them, but only adjust their magnitudes. E.g. for a spin designated "up", only positive values of $\langle J^z \rangle$ will be able to satisfy the self-consistent calculation.

3.2.1 Nonlinear Gauss-Seidel method

Although the local fields are linear functions of the magnetic moments as described in eq. (2.10), the magnetic moments are complicated nonlinear functions of the local fields, and are obtained by diagonalizing (3.1), choosing one of the two low energy states and then taking its expectation value $\langle J^z \rangle$. Hence the system of equations in question (3.2) is nonlinear, and no algorithm is guaranteed to reliably find a solution [17]. The Gauss-Seidel method is a classical iterative method for solving *linear* systems of equation, but we find that implementing a similar idea for our nonlinear problem was quite effective. The iterative step is defined by

$$x_i^{(l+1)} = g_{i\chi_i}(x_1^{(l+1)}, \dots, x_{i-1}^{(l+1)}, x_i^{(l)}, x_{i+1}^{(l)}, \dots, x_N^{(l)}) \quad (3.5)$$

where the superscripted index indicates the iteration number. In other words, the magnetic moment of the i th spin is set to its target value, based on the current values of other magnetic moments. Then, the new value is immediately used for setting the magnetic moment of the $(i + 1)$ th spin. All N values $\{x_1, \dots, x_N\}$ are set successively this way and then we proceed to the next iteration. In practice a relaxation parameter α is introduced so that

$$x_i^{(l+1)} = \alpha g_{i\chi_i}(x_1^{(l+1)}, \dots, x_{i-1}^{(l+1)}, x_i^{(l)}, x_{i+1}^{(l)}, \dots, x_N^{(l)}) + (1 - \alpha)x_i^{(l)} \quad (3.6)$$

This way, α allows us to control how drastically x_i values change at each iteration, where $\alpha = 1$ reduces eq. (3.6) back to eq. (3.5) and $\alpha = 0$ means the initial guess is never changed. Setting $1 < \alpha < 2$ is known as over-relaxation [17] and was not found to be useful for this problem. We found that setting $\alpha = 0.95$ gave the quickest convergence and best convergence success rates for this problem.

3.2.2 Newton's and Broyden's methods

A second class of iterative methods is one that tries to improve the entire solution vector $x = (x_1, \dots, x_N)$ simultaneously by taking into account the

derivatives of the functions f_i (3.2) as well as their values. The iteration steps are determined by expanding each of the functions in a Taylor series around \mathbf{x} ,

$$f_i(\mathbf{x} + \delta\mathbf{x}) = f_i(\mathbf{x}) + \sum_{j=0}^{N-1} \frac{\partial f_i}{\partial x_j} \delta x_j + O(\delta\mathbf{x}^2) \quad (3.7)$$

The partial derivatives matrix $J_{ij} \equiv \frac{\partial f_i}{\partial x_j}$ is known as the Jacobian matrix. Then, in order to get a step that brings each of the functions f_i closer to zero, we set $f_i(\mathbf{x} + \delta\mathbf{x}) = 0$. In matrix notation this means

$$0 = \mathbf{f}(\mathbf{x}) + \mathbf{J} \cdot \delta\mathbf{x} \quad (3.8)$$

which is a linear system of equations for $\delta\mathbf{x}$. The solution is used to update \mathbf{x} as in

$$\mathbf{x}^{(l+1)} = \mathbf{x}^{(l)} + \delta\mathbf{x} \quad (3.9)$$

Thus Newton's method involves calculating the Jacobian matrix, solving (3.8) and changing \mathbf{x} according to (3.9). The partial derivatives in \mathbf{J} are taken from the trilinear interpolation, where they have a relatively simple form (see appendix C). Broyden's method is an alternative to Newton's method that provides a computationally cheaper approximation of the Jacobian matrix that is also updated at each iteration. The exact procedure is detailed in Ref. [17, section 9.7.3]. Both of these methods are slightly modified so that the step in (3.9), is taken in the direction of $\delta\mathbf{x}$ but not necessarily by that size. The size of the step is instead determined so that the norm of the vector function squared, $\|\mathbf{f}(\mathbf{x})\|^2$, is optimally decreased. This modification is supposed to help achieve better *global* convergence [17, section 9.7].

The nonlinear Gauss-Seidel method is the first one attempted as it is the most efficient of the methods described. Only if it fails to converge to a solution is one of the other methods, i.e. Broyden's method or Newton's method, used.

Both the nonlinear Gauss-Seidel and Newton's and Broyden's methods are iterative in nature and thus require an initial state from which to start their operation. The obvious choice is to use the previous Monte Carlo state, i.e. the solution that was found for the previous spin configuration which differs from the current configuration by only the one spin that was flipped. This also allows us to introduce another modification to the algorithm that is used in case both of these methods fail to find a solution. The idea is to gradually flip the selected spin and continuously adjust the

solution so that it is valid at every step during the change. In practice this means that when flipping the i th spin, e.g. from $|\uparrow\rangle$ to $|\downarrow\rangle$, the function $g_{i\uparrow}$ is gradually changed to $g_{i\downarrow}$. For all methods, convergence is determined by the condition

$$\frac{1}{N} \sum_i^N |f_i(x_1, \dots, x_N)| < \epsilon_{\text{tol}} \quad (3.10)$$

where we set $\epsilon_{\text{tol}} = 5 \times 10^{-3}$.

3.3 Monte Carlo simulation

Monte Carlo simulation is a numerical method used extensively in statistical mechanics [18]. The Metropolis algorithm, introduced in 1953 by Metropolis *et al.*, is the most widely used Monte Carlo algorithm and the main tool used in this work. The algorithm is used to calculate thermal averages, that, in equilibrium, are given by the Boltzmann average

$$\langle Q \rangle_T = \frac{\sum_{\mu} Q_{\mu} e^{-E_{\mu}/kT}}{\sum_{\mu} e^{-E_{\mu}/kT}} \quad (3.11)$$

where the sum over μ is a sum over all possible states of the system, and Q_{μ} and E_{μ} are the value of the observable Q and the energy in the state μ respectively. The general idea behind the Metropolis algorithm is to create a new state from the previous one by modifying it slightly. If the transition probability between such successive states, μ and ν , obeys the detailed balance condition of

$$\frac{P(\mu \rightarrow \nu)}{P(\nu \rightarrow \mu)} = e^{-\beta(E_{\nu} - E_{\mu})} \quad (3.12)$$

then the equilibrium distribution of states produced by the described process will be the Boltzmann distribution. When we have a successive sequence of random states whose distribution is the Boltzmann distribution we may average any observable over that sequence to estimate eq. (3.11) (this is known as importance sampling) [18]. The Metropolis algorithm satisfies the condition (3.12) by choosing one spin at random and flipping it with the probability

$$A(\mu \rightarrow \nu) = \begin{cases} e^{-\beta(E_{\nu} - E_{\mu})} & \text{if } E_{\nu} - E_{\mu} > 0 \\ 1 & \text{otherwise} \end{cases} \quad (3.13)$$

where $A(\mu \rightarrow \nu)$ is the probability of accepting the new state ν , which is proportional to the transition probability $P(\mu \rightarrow \nu)$. In summary, the flow of the algorithm for the Ising model is as follows, given an initial state $\mu = \{s_i\}$ with energy E_μ where $\{s_i\}$ are the values of the spins,

1. Choose random spin s_i and flip it to get a new state
 $\nu = \{s_1, \dots, s_{i-1}, -s_i, s_{i+1}, \dots, s_N\}$
2. Calculate the energy of the new state E_ν
3. If $E_\nu < E_\mu$ accept the new state and go back to 1
4. If $E_\nu > E_\mu$ accept the new state with probability $e^{-\beta(E_\nu - E_\mu)}$ or reject it with probability $1 - e^{-\beta(E_\nu - E_\mu)}$ and return to 1.

We call the above process a Monte Carlo step, and N (the total number of spins) such Monte Carlo steps are called a Monte Carlo sweep (MCS). A MCS is the basic unit of time of the simulation and measurements of observables are taken after each such sweep. Continued iteration of the above algorithm would reach a steady-state in which the sequence of generated states obeys the Boltzmann distribution, and from which meaningful measurements can be taken. The two most important aspects of the simulation which must be taken into consideration to ensure that the measurements are valid are equilibration and autocorrelation. They will be discussed in the next two sections.

To calculate the energy of a state as required by the Metropolis algorithm, the Hamiltonian in (2.11) is used as follows: First its first two terms are used to self-consistently determine the expectation values $\langle J_1^z \rangle, \dots, \langle J_N^z \rangle$ (as explained in section 3.2), and then they are used to calculate the energy of the full Hamiltonian in (2.11).

3.3.1 Equilibration

The algorithm described in 3.3 starts from some initial configuration, which in our case we choose to be a random one, corresponding to $T \rightarrow \infty$. Thus we have no reason to assume that measurements performed in the first few MCS are representative of the system at the finite temperature that is currently being simulated. The time, in MCS, the simulation has to run until it reaches an equilibrium steady-state is called the equilibration

time, τ_{eq} . The way we determine τ_{eq} is by monitoring all measured observables as a function of MCS. We perform logarithmic binning of each measured observable, meaning that measurements are averaged over an exponentially increasing number of MCS. The i th bin, where $i = 0, 1, 2, \dots$, holds the average of measurements performed at MCS between $t_0 = 2^i - 1$ and $t_1 = 2t_0$ (MCS are numbered starting from zero). In figure 3.2 we show the equilibration process of two observables, energy per spin and magnetization. The two quantities are plotted as a function of MCS bin, where each point is the average of the corresponding quantity among the measurements in that bin. The error bars are the statistical errors of the measurements in the bin, calculated using the autocorrelation analysis described in the next section. An observable is assumed to be equilibrated once three consecutive bins agree within error bars [19]. As mentioned, only once all measured observables are equilibrated the system is considered equilibrated and measurements are used. The measured observables are the total energy, the magnetization per spin and the magnetization per spin squared, and the k -dependent magnetization, defined in (3.18), squared. Simulations of temperatures that did not meet this criterion ($< 2\%$) were not used in the final analysis.

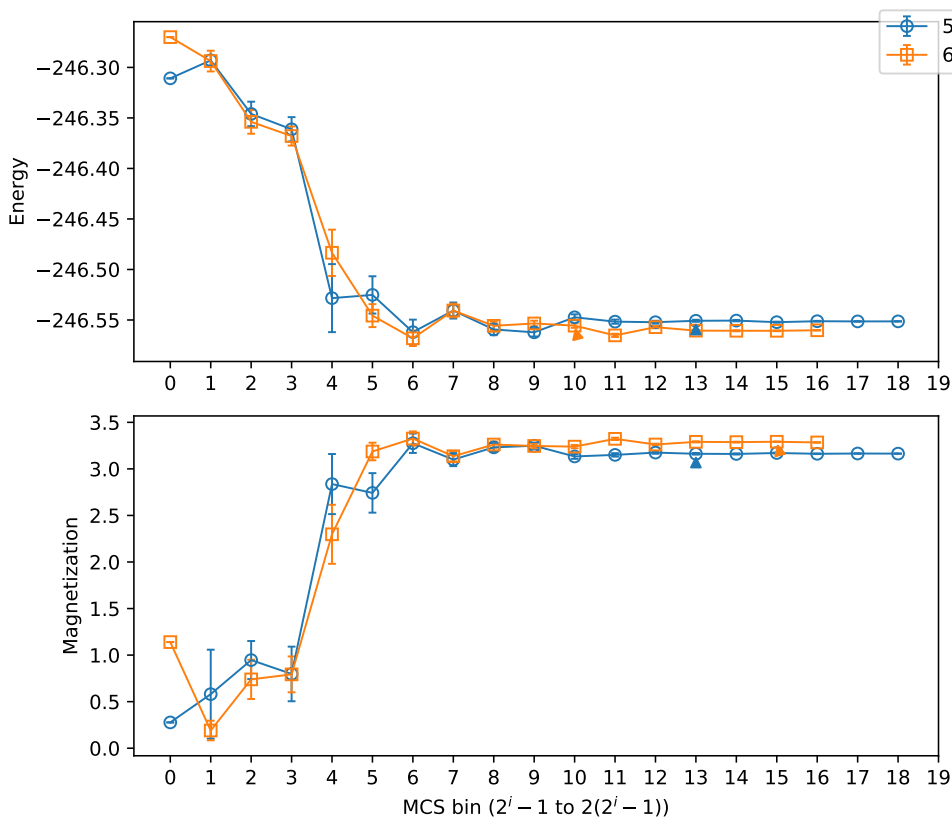


Figure 3.2: Example of equilibration process. The equilibration process for two observables, Energy per spin and total magnetization. Two system sizes are plotted, $L = 5, 6$, and other parameter values are $B_x = 0.0$, $T = 1.5$ and ODD terms are included. Small triangles mark the point of equilibration for each system size and each observable as determined by the conditions described in this section.

3.3.2 Autocorrelation

The Metropolis algorithm has the advantage that generating new states from previous ones by flipping a spin is relatively computationally easy, but this comes with a drawback that successive states are highly correlated. In contrast, two states that differ by a large enough number of MCS, which we denote τ_{auto} , may be assumed uncorrelated [18]. In order to address the issue of correlations we employ the so called "binning" or "blocking" method [20, 21], in which the data used is not the individual measurements but an average of them over a range of MCS called a "bin".

These should not be confused with the logarithmic bins described in section 3.3.1 that are used to monitor equilibration. Rather, these bins are made up of measurement taken after the system is deemed equilibrated. If the size of the bins is greater than τ_{auto} then we can use the bin averages as uncorrelated estimations of the observables of interest.

In practice the procedure we employ is as follows: Given a data set of measurements x_1, \dots, x_N , we create a new "binned" data set $x'_1, \dots, x'_{N/2}$ by averaging pairs of successive measurements. This process is performed iteratively so we can define it in terms of the "binning level" l such that

$$x_i^{(l)} := \frac{1}{2} \left(x_{2i-1}^{(l-1)} + x_{2i}^{(l-1)} \right) \quad (3.14)$$

where the zeroth level is the original data set. For each binning level, the standard error of the binned data set is computed, as well as its uncertainty (by bootstrap analysis, see sec. 3.3.3). The sequence of values for the standard error will increase until a fixed point is reached where the value remains roughly constant within error bars. This point signifies that the length of the bins is large compared to the autocorrelation time, so that correlations do not significantly affect the estimate of the error. For large binning levels, the data set becomes increasingly small and fluctuations of the error become very large. Therefore, when plotting the standard error vs. binning level, the fixed point appears as a distinct plateau, as can be seen in figure 3.3. We determine the existence of such a plateau by demanding three consecutive points that agree within error bars, and then taking the first binning level within that plateau as the one for which the binned data set is effectively uncorrelated. That is the data used in further analysis. If no such plateau is found, it is taken as a signal that the simulation has not run for long enough [21] and the largest value obtained for the standard error is considered a lower bound on that error [20].

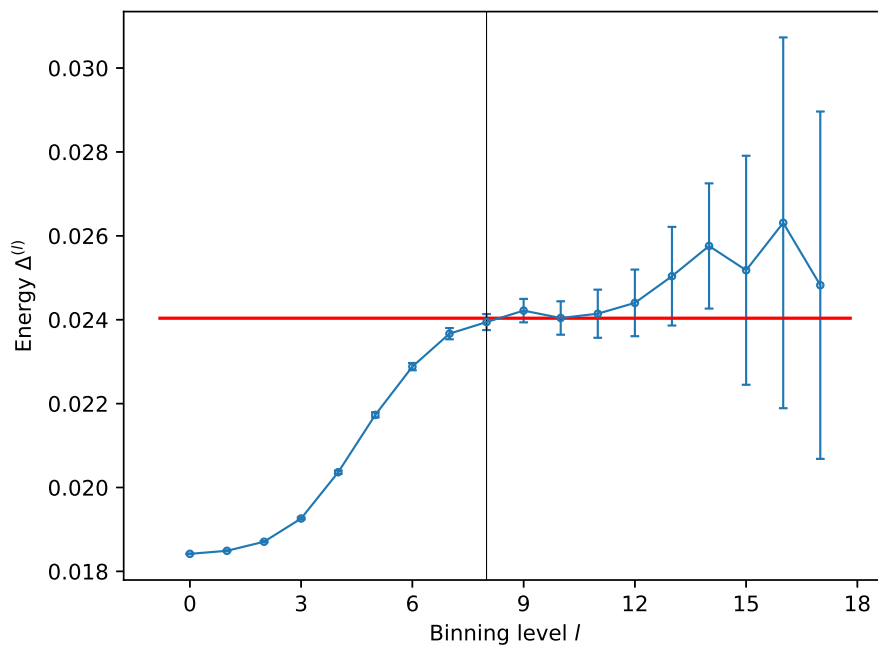


Figure 3.3: Example of binning analysis. The standard error of the energy (the measured observable in this example) within the binned array is plotted against the binning level. The red horizontal line indicates the asymptotic value of the error, determined by the plateau, and the vertical black line indicates the binning level at which we consider the bin averages uncorrelated. The simulation parameters are: $L = 4$, $B_x = 0.0$, $T = 1.47434$ and ODD terms are excluded.

3.3.3 Finite size scaling

A computer simulation is inherently limited by the available memory, and hence only finite systems may be simulated. We would still like to study the bulk characteristics of the system, which may be smeared out for systems that are not infinitely large. The finite size scaling method allows one to extract the values of critical exponents and the value of T_c by simulating systems of different sizes L and analyzing their results [18]. The non-analytic part of a given observable close to the critical temperature can be described by a finite-size scaling form. For example, the finite-size magnetization from a simulation of an Ising system is asymptotically given by

[18]

$$\langle m_L \rangle \sim L^{-\beta/\nu} \tilde{m}[L^{1/\nu}(T - T_c)] \quad (3.15)$$

where \tilde{m} is an unknown universal scaling function that is the same for all L . Thus, if we perform a set of Monte Carlo simulations for various different L , measure the magnetization over a range of temperatures around T_c , and plot $L^{\beta/\nu} \langle m_L \rangle_T$ as a function of the scaled variable $x = L^{1/\nu}(T - T_c)$, for a correct choice of ν , β and T_c , we should have all values fall on a single curve that would represent the universal function \tilde{m} . This technique can be improved by studying combined dimensionless quantities that do not require we know the critical exponents in advance. A notable example is the Binder ratio given by [22]

$$g = \frac{1}{2} \left[3 - \frac{\langle m^4 \rangle}{\langle m^2 \rangle^2} \right] \sim \tilde{G} \left(L^{1/\nu}(T - T_c) \right). \quad (3.16)$$

Another example for such a quantity, which is the one we use in this work, is the finite-size correlation length given by [22]

$$\tilde{\zeta}_L = \frac{1}{2 \sin(k_{\min}/2)} \left[\frac{\langle m^2(0) \rangle_T}{\langle m^2(\mathbf{k}_{\min}) \rangle_T} - 1 \right]^{\frac{1}{2}} \quad (3.17)$$

where

$$m(\mathbf{k}) = \frac{1}{N} \sum_{i=1}^N \langle J_i^z \rangle \exp(-i\mathbf{k} \cdot \mathbf{R}_i). \quad (3.18)$$

Here $\langle \cdot \rangle_T$ refers specifically to thermal average, \mathbf{R}_i is the location of the site i and $\mathbf{k}_{\min} = (\frac{2\pi}{L}, 0, 0)$. The finite-size correlation length divided by the linear system size has the same scaling form as the Binder ratio,

$$\frac{\tilde{\zeta}_L}{L} \sim \tilde{X} \left(L^{1/\nu}(T - T_c) \right) \quad (3.19)$$

so that for $T = T_c$ it is independent of the system size L . Therefore we can expect curves for different system sizes to cross at the critical temperature. The advantage of $\tilde{\zeta}_L/L$ over the Binder ratio is that the Binder ratio is restricted to the interval $[0, 1]$ while $\tilde{\zeta}_L/L$ is not, which makes the crossing of different curves clearer and more accurate [19]. To systematically get the values for T_c and the critical exponent ν , we assume the scaling functions (3.19) and (3.16) can be approximated by a third-order polynomial close to the critical point: $f(x) = p_0 + p_1x + p_2x^2 + p_3x^3$ (where $x = L^{1/\nu}(T - T_c)$), and perform a global fit for the six free parameters, $p_0 \dots p_3$, ν and T_c using the Levenberg-Marquardt algorithm [19].

Bootstrap analysis To estimate the error bars of T_c obtained by finite size scaling, we use the so called *bootstrap* method [18, section 3.4.3]. The exact procedure follows ref. [19]: For each size L and each temperature T , the averages in eq. (3.16) and eq. (3.17) are calculated from a resampled data set rather directly than from the data set of Monte Carlo results. This new dataset is obtained from the Monte Carlo data set of size N_{MC} by choosing at random N_{MC} measurements **with replacement**, so that the same measurement may be picked more than once. The new dataset is used to calculate either the Binder ratio or the correlation length for each L and T , and then they are fitted to obtain the free parameters as described above. This is then repeated $N_{boot} = 500$ times so that we have N_{boot} different estimates of these parameters. The estimated errors of the parameters are then given by the standard deviation among the N_{boot} bootstrap samples. The data set which is resampled in this case has already been processed as described in the previous sections so that it is considered to consist of independent measurements describing the equilibrium values of the measured observables.

4 Results

The results of the Monte Carlo simulations are presented in this chapter. As the purpose of the simulations is to estimate the significance of the proposed mechanism of offdiagonal dipolar terms causing a decrease in T_c , the simulations are performed twice: Once with the offdiagonal dipolar terms included in the Hamiltonian (2.11) and once with these terms omitted so that internal transverse fields are artificially suppressed. This is done by explicitly setting $B_i^x = B_x$ and $B_i^y = 0$ for all i in (2.10). In this case the self consistent calculation described in 3.2 becomes trivial, but it is performed as described nonetheless with the purpose of establishing its validity.

The process from which the following results are obtained is as follows: The value of B_x is set, and then a range of temperatures around T_c is simulated for several system sizes. These simulations are used to obtain the averages required to calculate the finite-size correlation length ξ_L which is used in the finite-size scaling method to obtain an exact estimate of T_c . Figures 4.1–4.4 show the finite-size scaling results. The dimensionless quantity ξ_L/L plotted in these figures is expected to scale as $\xi_L/L \sim \tilde{X} [L^{1/\nu}(T - T_c)]$. At the critical temperature $T = T_c$, the argument of the scaling function is zero, and hence independent of L , so all lines for different system sizes are expected to cross at this temperature. As can be seen in (a) of all of these figures, the lines indeed cross, but at noticeably different points for different pairs of L s. This is most likely due to corrections to finite-size scaling that are significant for small system sizes where the scaling expressions used to determine exponents do not work well enough [18, 19]. In principle one can find a better estimate of the critical temperature by calculating it for pairs of distinct system sizes, e.g. $T_c^*(L, 2L)$ and estimating the limit value of $L \rightarrow \infty$. Unfortunately we could not simulate larger system sizes than what is presented due to the computational complexity of the algorithm used. Therefore we take these corrections as given, and incorporate them into our error estima-

tions explicitly, since they are systematic rather than statistical errors and are not expected to be incorporated by the bootstrap error estimation (see section 3.3.3). Hence, the difference between the crossing of $L = 4, 5$ and $L = 5, 6$ is added to the error bars as a rough estimate of the error introduced by the scaling corrections. Despite these corrections, all figures show reasonable collapse to a universal curve as can be seen in (b).

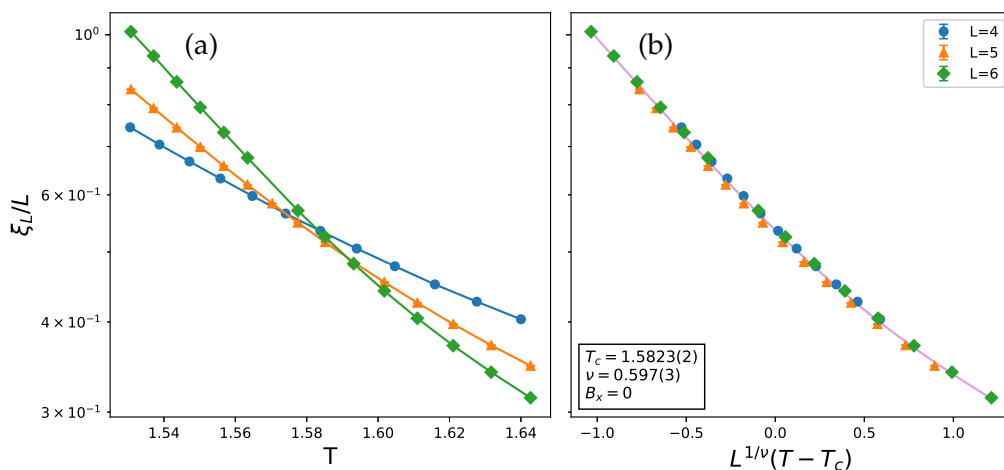


Figure 4.1: Finite size correlation length ξ_L/L as a function of the temperature for different linear system sizes L . Data is for $B_x = 0.0$ and internal fields unsuppressed so that the mechanism is active. (a) Shows the crossing of different system sizes. (b) Scaling analysis of the data. The solid line corresponds to the optimal scaling function based on a polynomial approximation.

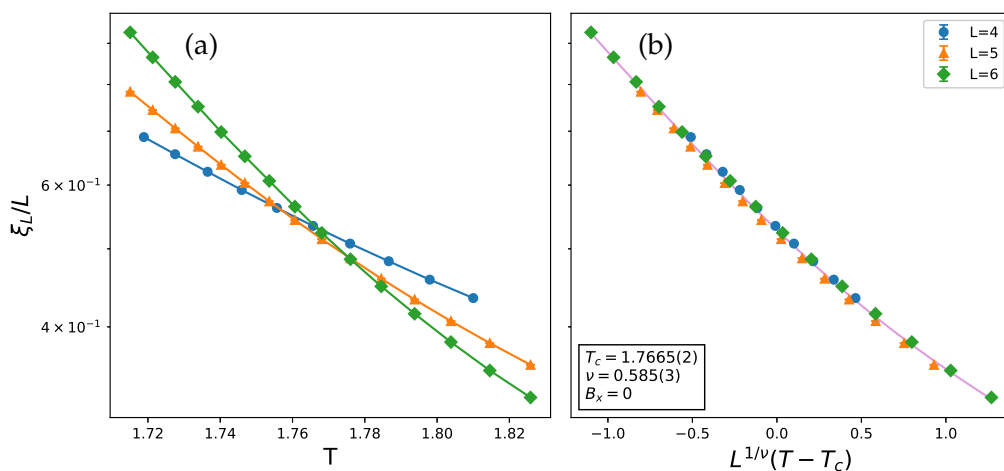


Figure 4.2: Finite size correlation length ξ_L/L as a function of the temperature for different linear system sizes L . Data is for $B_x = 0.0$ and internal fields suppressed so that the mechanism is inactive. (a) Shows the crossing of different system sizes. (b) Scaling analysis of the data. The solid line corresponds to the optimal scaling function based on a polynomial approximation.

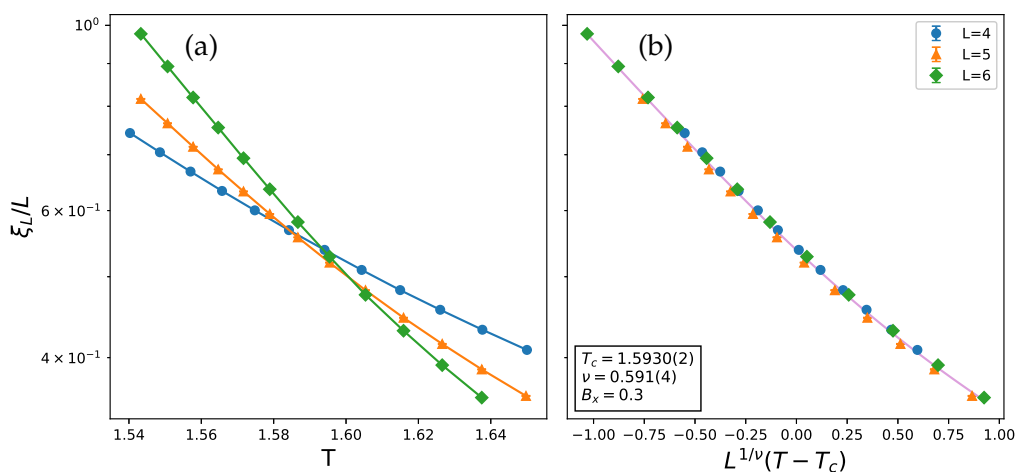


Figure 4.3: Finite size correlation length ξ_L/L as a function of the temperature for different linear system sizes L . Data is for $B_x = 0.3$ T and internal fields unsuppressed so that the mechanism is active. (a) Shows the crossing of different system sizes. (b) Scaling analysis of the data. The solid line corresponds to the optimal scaling function based on a polynomial approximation.

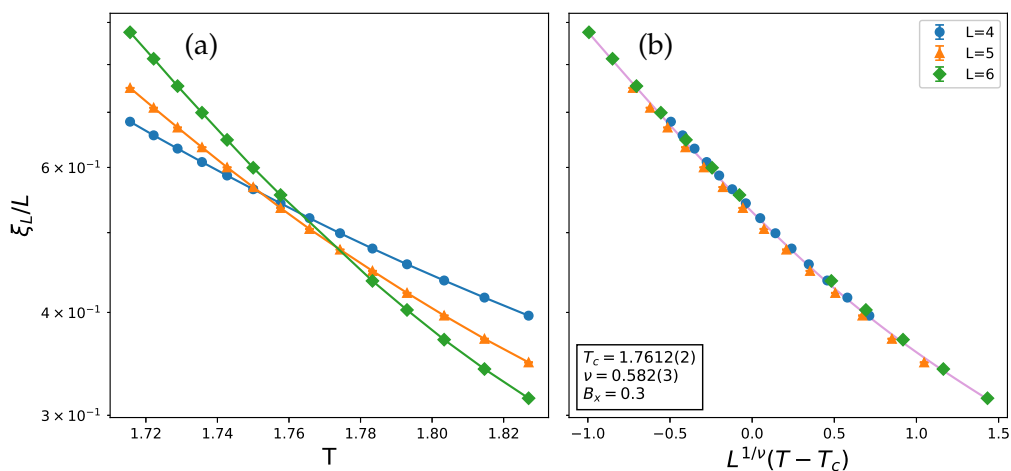


Figure 4.4: Finite size correlation length ξ_L/L as a function of the temperature for different linear system sizes L . Data is for $B_x = 0.3$ T and internal fields suppressed so that the mechanism is inactive. (a) Shows the crossing of different system sizes. (b) Scaling analysis of the data. The solid line corresponds to the optimal scaling function based on a polynomial approximation.

The values of T_c obtained by the finite-size scaling procedure are then plotted on the full phase diagram in figure 4.5. The inset of the figure shows the low- B_x region closer up, where it is more obvious that the difference between T_c obtained with and without the ODD terms decreases as B_x is increased. On the inset to the right the results without ODD terms can be seen to be compatible with the mean field result, though it is consistently lower, which might be attributed to finite size effects. On the inset to the left, the results with the ODD terms can be seen to also overestimate T_c compared to experiment, albeit by a much smaller amount. The result for $B_x = 0.3$ T is, surprisingly, higher than that for $B_x = 0$ which will be discussed in the next section.

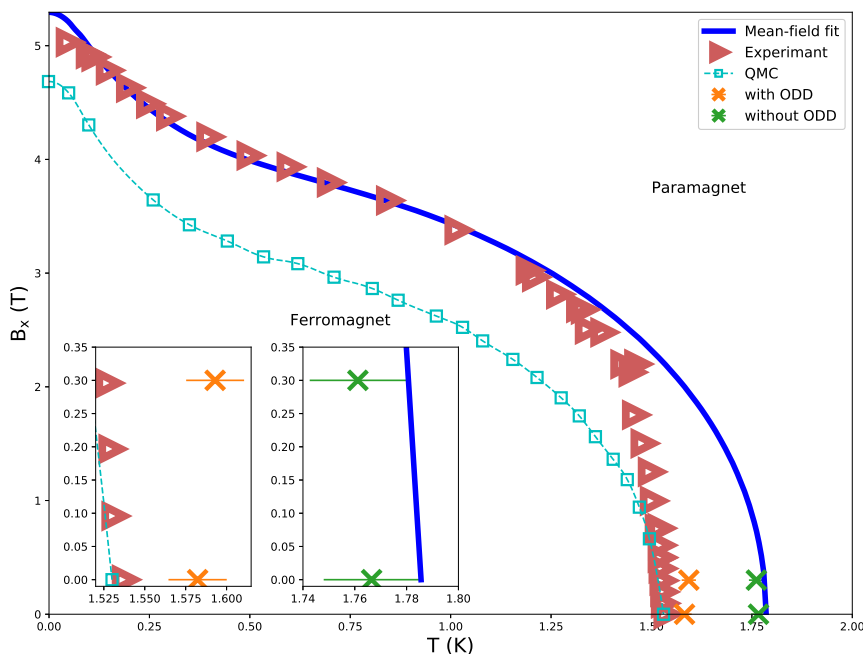


Figure 4.5: Phase diagram of LiHoF_4 with numerical results. Experimental data (triangles) and mean-field fit (solid line) from ref. [5]. Quantum Monte Carlo (QMC) data (open squares) is from ref. [3]. The Xs are the numerical results of this work, where orange is for simulations with offdiagonal dipolar terms included and green is for simulations where they are excluded. The inset shows the low- B_x region of both results, where the behavior at $B_x = 0.3$ T relative to $B_x = 0.0$ T can be seen more clearly. All numerical results use $J_{\text{ex}} = 1.16 \times 10^{-3}$ K.

4.1 Discussion

The numerical results presented above clearly show that inclusion of the ODD terms leads to a significant decrease of T_c , which is of the order of magnitude that separates the mean-field T_c obtained by Babkevich et al. [5] from the experimental value. This fact suggests that these terms may account for the discrepancy between previous theoretical predictions and experimental data. All results presented in this chapter use the exchange parameter suggested by Rønnow et al. [4] of $J_{\text{ex}} = 1.16$ mK. This ex-

change parameter produces mean-field results that agree with experimental results for $B_x > 3$ T but give $T_c(0)$ much larger than the experimental value. Therefore, we suggest that this is the correct value of J_{ex} , and that the mechanism described in section 2.5 is the one that lowers T_c to its experimental value in the real LiHoF_4 . This mechanism fundamentally relies on the actual configuration of the spins and therefore is not expected to be represented in any mean-field description. As additional support for this hypothesis, figure 4.6 shows the standard deviation of the internal transverse fields, B_x^i , over all sites as a function of temperature. It can clearly be seen that the standard deviation, and hence the typical value of the local transverse field, increases with temperature, which is consistent with the heuristic argument given in section 2.5.

A second important observation is that the difference between the numerical results with and without the ODD terms is smaller for $B_x = 0.3$ T. This may explain the $T_c(B_x)$ dependence, in that it suggests the mechanism is attenuated by increasing the external B_x .

Of course, the numerical results, even with ODD terms included, do not agree with the experimental ones. One possible reason for this lies in the interpolation scheme described in section 3.1. As can be seen in the left graph of figure 3.1, for values $|B_z| < 0.029$ T, the interpolated function is roughly constant at about $\langle J^z \rangle \approx \pm 5\mu_B$ while the actual function goes rapidly to zero. This would mean that in the course of the simulation higher expectation values are assigned to the spins in that B_z region than what is actually dictated by the applied local field. Roughly speaking, since the J^z expectation values act as effective magnitudes of the spins, such an artificial increase in their values would raise T_c . This issue becomes more significant with higher applied transverse field, whether internal or external, since the B_z region affected by this becomes larger. Consequently, the issue should affect simulations with ODD terms included more as their local transverse fields consist of external as well internal fields. This is true also for $B_x = 0$ where the issue does not exist at all without ODD terms, but it does when they are included. This would explain why simulations without ODD terms give $T_c(0)$ approaching the mean-field prediction (up to scaling corrections), while with ODD terms they give $T_c(0)$ that is higher than the experimental result.

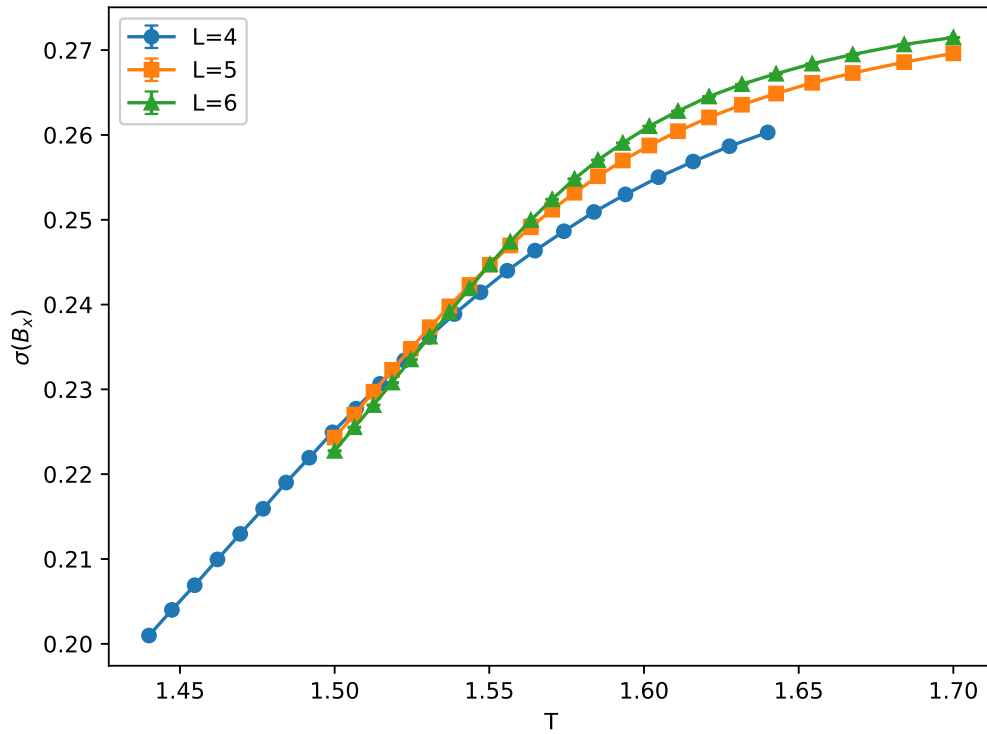


Figure 4.6: The standard deviation of local transverse fields B_i^x among all H_0 sites as a function of temperature. $B_x = 0.0$ T, ODD terms included. Similar behaving results are obtained for $B_x > 0.0$ T as well.

5 Summary

In this work we have numerically studied the phase transition of LiHoF_4 under applied transverse external field B_x , at the low- B_x region. The main hypothesis presented was that correct treatment of the offdiagonal terms of the dipolar interaction could account for the discrepancy between theory and experiment in the low- B_x regime.

Using Monte Carlo simulations we found that inclusion of these terms in the studied Hamiltonian leads to a significant decrease of T_c at zero-transverse field. The decrease is of the correct order of magnitude required to explain the discrepancy between the mean-field solution and experimental results. In addition, we have shown that at $B_x > 0$, the diminishing of T_c as a result of the offdiagonal dipolar terms becomes less effective. This is consistent with our hypothesis, as the discrepancy also diminishes with increasing B_x . Furthermore, our results provide support to the determination of J_{ex} based on the high- B_x regime, as was done in ref. [5].

However, exact agreement with experimental data in the low- B_x region could not be achieved. This might partly be due to the limited range of system sizes used in this work, but may also point to an issue with the simulation procedure as discussed in section 4.1.

There are several avenues for further work based on these results. First, it would be crucial to confirm or refute the suggestion raised in section 4.1 that the cause of the remaining discrepancy lies in the interpolation scheme. This could be done, e.g. by varying the minimal B_z value from which the magnetic moment is interpolated (currently $|B_z| = \pm 0.029$ T), and monitoring its affect on T_c . Second, running more simulations to obtain additional points at $B_x > 0$, with and without the ODD terms, could further support the claim that the effect is diminished with increasing B_x , and hopefully reproduce the correct phase boundary shape. Lastly, in order to explore larger system sizes than currently possible, a different

model might prove useful. For example, a model with short-range interactions, as opposed to the long-range dipolar interactions currently used, should be considerably easier to simulate. Such a model could be formulated simply by truncating the dipolar interactions at some distance. One would obviously not expect such a model to give the exact same values of T_c , but it might be used to study the $T_c(B_x)$ dependence nonetheless.

A Single Ho^{3+} Ion and Crystal properties

A.1 Single Ion Electronic States

The Ho ions in the LiHoF_4 crystal are trivalent, so that each ion has 10 electrons in its unfilled $4f$ shell ($4f^{10}$) [3]. The spatial extent of the $4f$ shell means that for rare earth ions, the crystalline environment does not significantly change the free states, so that they may be treated as isolated ions [23]. Thus we apply Hund's rules to find the ground state electronic configuration, which gives $J = 8$ ($L = 6$, $S = 2$), denoted 5I_8 . There is strong spin-orbit coupling [7], so the z projections of the total orbital angular momentum L and total spin S are not good quantum numbers. Instead, the total angular momentum J and its projection J^z are used to characterize the electronic states, which gives rise to a 17-fold degenerate ground state with a Landé g -factor of $g_L = \frac{5}{4}$ [7, 23]. Interactions of the Ho^{3+} ions with the Li^+ and F^- ions lift the degeneracy, as will be discussed in the next section.

A.2 Crystal Field Hamiltonian

The Coulomb interactions of the Ho^{3+} ions with the Li^+ and F^- ions can be captured in the crystal field Hamiltonian, V_C , which can be approximately constructed based on the symmetry of the crystal [24]. The approximated model used is known as the *point-charge* approximation. In essence it amounts to treating other ions as point charges, thus neglecting the finite spatial extent of their charge. Additionally, it neglects the overlap of the magnetic ions' wave functions with those of their neighbors, and screening by electrons in outer shells. Its power lies in preserving the symmetry

of the crystal, which enables us to easily expand it in terms of functions that possess the same symmetries of the crystal. Under this approximation the electrostatic potential $V(r, \theta, \phi)$ due to the surrounding point charges, at point (r, θ, ϕ) near the origin at the ion is

$$V(r, \theta, \phi) = \sum_j \frac{q_j}{|\mathbf{R}_j - \mathbf{r}|} \quad (\text{A.1})$$

where q_j is the total charge of the j th ion, that is at location \mathbf{R}_j relative to the origin. In order to take advantage of the symmetry of the crystal, the potential is expanded in terms of tesseral harmonics, which are a real form of spherical harmonics [24]. Using the notation of Prather [25], the potential (A.1) takes the form

$$V(r, \theta, \phi) = \sum_j q_j \sum_{n=0}^{\infty} \frac{r^n}{R_j^{(n+1)}} \frac{4\pi}{(2n+1)} \sum_{m=0}^n [C_n^m(\theta, \phi) C_n^m(\theta_j, \phi_j) + S_n^m(\theta, \phi) S_n^m(\theta_j, \phi_j)] \quad (\text{A.2})$$

where C_n^m and S_n^m are tesseral harmonics (a list of which is given in ref. [25, Table 2]). The potential can be written as

$$V(r, \theta, \phi) = \sum_{n=0}^{\infty} r^n \sum_{m=0}^n [A_n^m C_n^m(\theta, \phi) + B_n^m S_n^m(\theta, \phi)] \quad (\text{A.3})$$

where A_n^m and B_n^m are constants involving sums over all other crystal ions. Some of these coefficients can and in fact must vanish, so that the potential function can reflect the point symmetry of the crystal as it should. Prather [25] investigates the symmetry possessed by the tesseral harmonics, and lists the ones that could give a non-vanishing contribution to the potential function for different point symmetry groups.

LiHoF₄ has S_4 point symmetry through the Ho ions, which means that it is invariant with respect to a rotation of $\frac{\pi}{2}$ about the z -axis followed by reflection with respect to the $x - y$ plane [2, 23].

Following ref. [25] we can then list the tesseral harmonics that appear in the expansion of the potential in (A.3). In fact not all tesseral harmonics that respect the crystalline symmetry are relevant; Some of them only couple electronic states that belong to excited configurations and are therefore neglected¹, and others have vanishing matrix elements between electronic states due to selection rules of integrals of spherical harmonics [24].

¹The lowest excited electronic configuration, 5I_7 , lies approximately 7400 K above the ground state configuration [3], so this is well justified in the temperature range of interest for this work.

For evaluating the matrix elements of the crystal field potential between coupled wave functions within the J manifold we use the method of *operator equivalents* developed by Stevens [26]. The method uses the Wigner-Eckhart theorem to replace tensor operators, such as x , y and z , by angular momentum operators J_x , J_y and J_z within the given J subspace. Because the angular momentum operators do not commute like their spatial counterparts, products of x , y and z must be replaced by a sum of products of all different permutations of J_x , J_y and J_z , divided by the number of such permutations. This gives an operator that is proportional to the original operator. Thus, the tesseral harmonics that remain in the expansion of the crystal field potential can be written in Cartesian coordinates, and then transformed to angular momentum operators according to this method. The relevant operator equivalents in the case of LiHoF_4 are [3]

$$O_2^0 = 3J_z^2 - J(J+1) \quad (\text{A.4a})$$

$$O_4^0 = 35J_z^4 - 30J(J+1)J_z^2 + 25J_z^2 - 6J(J+1) + 3J^2(J+1)^2 \quad (\text{A.4b})$$

$$O_4^4(C) = \frac{1}{2} (J_+^4 + J_-^4) \quad (\text{A.4c})$$

$$\begin{aligned} O_6^0 = & 231J_z^6 - 315J(J+1)J_z^4 + 735J_z^4 + 105J^2(J+1)^2J_z^2 \\ & - 525J(J+1)J_z^2 + 294J_z^2 - 5J^3(J+1)^3 \\ & + 40J^2(J+1)^2 - 60J(J+1) \end{aligned} \quad (\text{A.4d})$$

$$O_6^4(C) = \frac{1}{4} (J_+^4 + J_-^4) (11J_z^2 - J(J+1) - 38) + \text{h.c.} \quad (\text{A.4e})$$

$$O_6^4(S) = \frac{1}{4i} (J_+^4 - J_-^4) (11J_z^2 - J(J+1) - 38) + \text{h.c.} \quad (\text{A.4f})$$

and the final crystal field Hamiltonian is

$$\begin{aligned} V_C = & B_2^0 O_2^0 + B_4^0 O_4^0 + B_6^0 O_6^0 + B_4^4(C) O_4^4(C) \\ & + B_6^4(C) O_6^4(C) + B_6^4(S) O_6^4(S) \end{aligned} \quad (\text{A.5})$$

where the coefficients B_l^m are known as crystal field parameters (CFPs), and are generally found by fitting to experimental data. In this work we use the CFPs suggested by Rønnow et al. [4] that in addition to susceptibility measurements [13] also incorporate results from several spectroscopic

investigations. Their values are

$$\begin{aligned}
 B_2^0 &= -0.696 \text{ K} \\
 B_4^0 &= 4.06 \times 10^{-3} \text{ K} \\
 B_4^4(C) &= 0.0418 \text{ K} \\
 B_6^0 &= 4.64 \times 10^{-6} \text{ K} \\
 B_6^4(C) &= 8.12 \times 10^{-4} \text{ K} \\
 B_6^4(S) &= 1.137 \times 10^{-4} \text{ K}
 \end{aligned} \tag{A.6}$$

The only terms in (A.5) that break z axis rotation symmetry are $B_4^4 O_4^4$ and $B_6^4 O_6^4$, that mix free states with $\Delta M_J = \pm 4$. Therefore eigenstates of the crystal field Hamiltonian are linear combinations of either $|\pm 7\rangle, |\pm 3\rangle, |\mp 1\rangle$ and $|\mp 5\rangle$; $|\pm 6\rangle, |\pm 2\rangle, |\mp 2\rangle$ and $|\mp 6\rangle$; or $|\pm 8\rangle, |\pm 4\rangle, |0\rangle, |\mp 4\rangle$ and $|\mp 8\rangle$ [7]. Figure A.1 shows the energy levels of the crystal field Hamiltonian vs. their J_z expectation value.

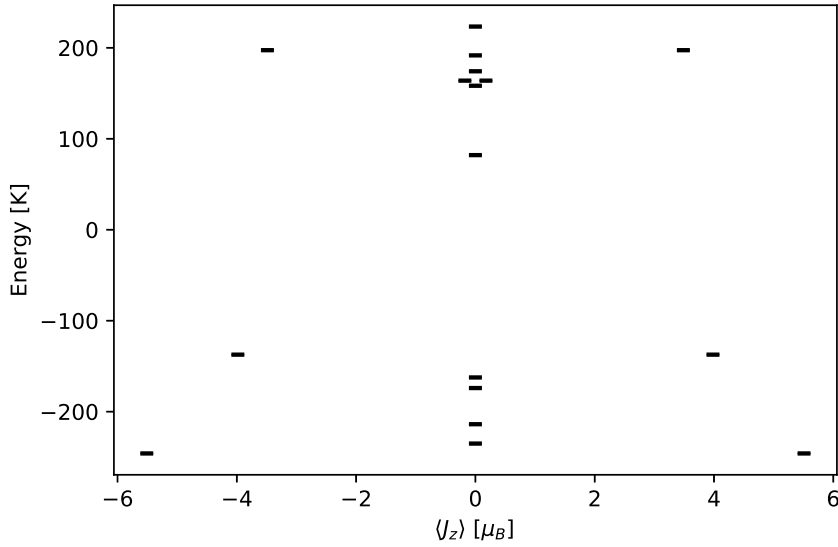


Figure A.1: Energy levels vs. the expected value of J_z , in zero applied field, under the crystal field potential (A.5). Obtained by numerical diagonalization. The low-energy Ising doublet can be seen, as well as the first excited singlet at ≈ 11 K above it.

B Ewald Summation Method

In order to incorporate the long-range dipolar interaction of eq. (2.2) we simulate the system with periodic boundary conditions. In this way, the system is considered to be surrounded by periodic copies of itself in every direction. Within this framework the effective interaction between a pair of spins consist not only of the direct dipolar interaction between them, but also of the dipolar interaction between all periodic copies of those spins. The method chosen to calculate these effective interactions is the Ewald summation method which is considered very useful for calculating long range dipolar interactions [9, 27]. The sum we wish to calculate is

$$V_{ij}^{\mu\nu} = \sum'_{\mathbf{n}} \frac{\delta_{ij}(\mathbf{r}_{ij} + \mathbf{n})^2 - 3(\mathbf{r}_{ij} + \mathbf{n})^\mu(\mathbf{r}_{ij} + \mathbf{n})^\nu}{|\mathbf{r}_{ij} + \mathbf{n}|^5} \quad (\text{B.1})$$

The prime symbol indicates that for $i = j$ the sum does not include the $\mathbf{n} = 0$ term. The sum in (B.1) is conditionally convergent, meaning that the result depends on the order of summation [27], which is why the Ewald method is required. In the Ewald method we separate this sum into two convergent sums: one in real space and the other in reciprocal space. A derivation of the technique is presented in ref. [27], here we shall only present the final forms used in this work, using the notation found in ref. [28]:

$$V_{ij}^{\mu\nu} = \sum'_{\mathbf{n}} \frac{\delta_{\mu\nu} B(r_{ij}) r_{ij}^2 - C(r_{ij}) r_{ij}^\mu r_{ij}^\nu}{r_{ij}^5} + \frac{4\pi}{L^3} \sum_{\mathbf{K} \neq 0} \frac{K_\mu K_\nu}{K^2} e^{-K^2/4\alpha^2} e^{i\mathbf{K} \cdot \mathbf{r}_{ij}} - \frac{4\alpha^3}{3\sqrt{\pi}} \delta_{\mu\nu} \delta_{ij} \quad (\text{B.2})$$

where

$$B(r) = \text{erfc}(r) + \frac{2\alpha r}{\sqrt{\pi}} e^{-\alpha^2 r^2} \quad (\text{B.3a})$$

$$C(r) = 3\text{erfc}(r) + \frac{2\alpha r(3 + 2\alpha^2 r^2)}{\sqrt{\pi}} e^{-\alpha^2 r^2} \quad (\text{B.3b})$$

\mathbf{K} are reciprocal lattice vectors and $\mathbf{n} = L(k\hat{x} + l\hat{y} + m\hat{z})$ where k, l, m are integers and $\hat{x}, \hat{y}, \hat{z}$ are unit vectors. $\text{erfc}(x)$ is the complementary error function. The first term in (B.2) is the real space sum, the second is the reciprocal space sum and the third is a self interaction term that represents the interaction of a spin with its periodic images. Another term which accounts for the polarization of the surface may be introduced in order to model different system shapes, however for the case of a long, cylindrical shape which we are considering, this surface term is zero [29]. We calculate the real and reciprocal sums by truncating them at $N_{\text{cutoff}}^{\text{real}}$ and $N_{\text{cutoff}}^{\text{reciprocal}}$ respectively. For the real sum, $N_{\text{cutoff}}^{\text{real}}$ is the absolute value of the cutoff in each direction, so that in practice $(2N_{\text{cutoff}}^{\text{real}} + 1)^3$ vectors are summed. For the reciprocal sum only half as many terms need to be summed after changing the complex exponential to a cosine function. Equation (B.2) is valid for any choice of α , but numerical convergence of the real and reciprocal sums depend strongly on the choice of α . Hence, α is chosen by plotting the slowest converging case, which was found to be the zz self interaction, once with $N_{\text{cutoff}}^{\text{real}}$ held constant and an increasing sequence of $N_{\text{cutoff}}^{\text{reciprocal}}$ s and then vice versa. Such plots are shown in figure B.1, and they allow us to optimally choose α such that it balances the convergence of the reciprocal and real parts. Based on this procedure we choose $\alpha = 2/L_z$ for all L . For that α , Both $N_{\text{cutoff}}^{\text{reciprocal}}$ and $N_{\text{cutoff}}^{\text{real}}$ are increased gradually until a combination is found for which no additional increase in either $N_{\text{cutoff}}^{\text{reciprocal}}$ or $N_{\text{cutoff}}^{\text{real}}$ changes the results. At this stage not only the zz self interaction but all types of interactions with all nearest neighbors are monitored. The resulting interactions are calculated once for each system size and saved to be used in simulations. Therefore computing time is less of a concern which allows us to set the cutoffs much higher than necessary. The values chosen are $N_{\text{cutoff}}^{\text{reciprocal}} = 12$ and $N_{\text{cutoff}}^{\text{real}} = 10$.

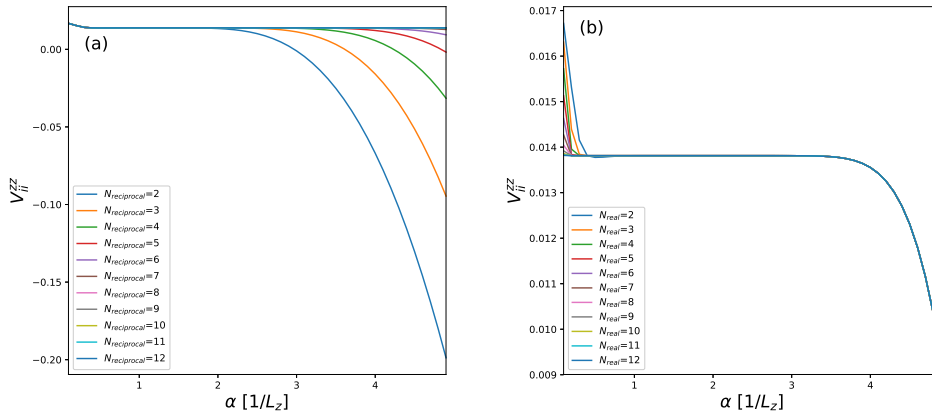


Figure B.1: Convergence tests of the Ewald sums

V_{ii}^{ZZ} calculated using the Ewald summation method as in (B.2) for $L = 6$.
 (a) N_{cutoff}^{real} is held constant at 2 and (b) $N_{cutoff}^{reciprocal}$ is held constant at 6.

C Interpolation

In this appendix we present the technical details of the trilinear interpolation that is used to obtain approximations of $\langle J^z \rangle$ and the energy, from the single-site Hamiltonian, as a function of the applied local magnetic field. For the sake of abstraction we use $f(x, y, z)$, x , y , z for the approximated function (either the energy or magnetic moment in our case) and its variables (B_x , B_y and B_z in our case). The closest values to (x, y, z) for which the function was calculated in advance are denoted (x_1, y_1, z_1) and (x_2, y_2, z_2) where $x_1 < x < x_2$ and likewise for y and z . This defines a grid cube that contains the point (x, y, z) . The interpolation then consists of four linear interpolations along the four edges of the cube parallel to the x axis [17],

$$\begin{aligned} R_{11} &= \frac{x_2 - x}{x_2 - x_1} f(x_1, y_1, z_1) + \frac{x - x_1}{x_2 - x_1} f(x_2, y_1, z_1) \\ R_{21} &= \frac{x_2 - x}{x_2 - x_1} f(x_1, y_2, z_1) + \frac{x - x_1}{x_2 - x_1} f(x_2, y_2, z_1) \\ R_{12} &= \frac{x_2 - x}{x_2 - x_1} f(x_1, y_1, z_2) + \frac{x - x_1}{x_2 - x_1} f(x_2, y_1, z_2) \\ R_{22} &= \frac{x_2 - x}{x_2 - x_1} f(x_1, y_2, z_2) + \frac{x - x_1}{x_2 - x_1} f(x_2, y_2, z_2) . \end{aligned}$$

This gives interpolated values of the function on four points along these edges that define a square containing the point (x, y, z) . Then, we perform linear interpolation along two edges of this square parallel to the y axis,

$$\begin{aligned} Q_1 &= \frac{y_2 - y}{y_2 - y_1} R_{11} + \frac{y - y_1}{y_2 - y_1} R_{21} \\ Q_2 &= \frac{y_2 - y}{y_2 - y_1} R_{12} + \frac{y - y_1}{y_2 - y_1} R_{22} . \end{aligned}$$

Lastly, we then perform linear interpolation between the two points found in the previous step, along the z axis,

$$f(x, y, z) = Q_1 + \frac{z - z_1}{z_2 - z_1}(Q_2 - Q_1). \quad (\text{C.1})$$

The order in which the interpolation steps along the three axes are performed is arbitrary, and may be switched when needed. This is useful, e.g. when the partial derivative of the function with respect to one of its variables is needed. In this case, for example, it is easy to identify $\frac{\partial f}{\partial z} = \frac{Q_2 - Q_1}{z_2 - z_1}$.

In practice we set up two interpolation tables, one for the energy and one for the magnetic moment, both of the $|\uparrow\rangle$ state. The energy and magnetic moment of the $|\downarrow\rangle$ state may then be obtained from the table by making the transformation $B_z \rightarrow -B_z$:

$$\langle \uparrow (B_x, B_y, B_z) | J^z | \uparrow (B_x, B_y, B_z) \rangle = - \langle \downarrow (B_x, B_y, -B_z) | J^z | \downarrow (B_x, B_y, -B_z) \rangle$$

$$\begin{aligned} \langle \uparrow (B_x, B_y, B_z) | H_{\text{single-site}} | \uparrow (B_x, B_y, B_z) \rangle = \\ \langle \downarrow (B_x, B_y, -B_z) | H_{\text{single-site}} | \downarrow (B_x, B_y, -B_z) \rangle \quad (\text{C.2}) \end{aligned}$$

D Numerical Parameters

In this section we detail the numerical parameters used in the simulations performed as part of this work. In all tables in this section L is the linear system size, T is the temperature, N_{mc} is the total number of MCS, N_{eq} is the number of MCS until equilibration and N_{eff} is the number of effective independent measurements after accounting for correlations. The last two are determined by a process detailed in sections 3.3.1 and 3.3.2 respectively.

Table D.1 summarizes the results presented in chapter 4. The errors listed for T_c are only the statistical errors. Errors plotted in figure 4.5 include errors stemming from finite-size corrections that are estimated as the difference between corresponding results for $L = 4, 5$ and $L = 5, 6$, as explained in chapter 4.

All other tables in this section detail the total number of MCS, number of MCS until equilibration and the effective number of measurements for each temperature and each linear system size simulated.

Table D.1: Summary of simulation results. Only statistical errors are given for T_c ; Errors stemming from finite-size corrections are estimated as the difference between corresponding results for $L = 4, 5$ and $L = 5, 6$ as explained in chapter 4.

L	B_x	T_c	ODD terms
4,5	0	1.7565(1)	excluded
4,5	0.3	1.7522(1)	excluded
4,5	0	1.5730(1)	included
4,5	0.3	1.5838(1)	included
5,6	0	1.7748(4)	excluded
5,6	0.3	1.7706(4)	excluded
5,6	0	1.5906(3)	included
5,6	0.3	1.6013(4)	included
4,5,6	0	1.7665(2)	excluded
4,5,6	0.3	1.7612(2)	excluded
4,5,6	0	1.5823(2)	included
4,5,6	0.3	1.5930(2)	included

Table D.2: Simulation parameters for $L = 4$, $B_x = 0.0$, without ODD terms

L	T	N_{mc}	N_{eq}	N_{eff}
4	1.61	2097152	16383	16256
	1.61757			16256
	1.62507			16256
	1.63252			16256
	1.63999			16256
	1.64751			16256
	1.65508			16256
	1.66269			16256
	1.67037			16256
	1.67812			8128
	1.68597			8128
	1.69397			8128
	1.70213			4064
	1.71044			8128
	1.71887			8128
	1.72751			8128
	1.73651			8128
	1.74594			8128
	1.75568			8128
	1.76566			2032
	1.77593			2032
	1.78661			2032
	1.79796			4064
	1.81			4064

Table D.3: Simulation parameters for $L = 5$, $B_x = 0.0$, without ODD terms

L	T	N_{mc}	N_{eq}	N_{eff}
5	1.69	1275000	32767	2420
	1.69635			605
	1.70263			2426
	1.70886			1213
	1.71508			1213
	1.72131			2426
	1.72756			4852
	1.73386			2426
	1.74026			4852
	1.7468			4852
	1.75357			4852
	1.76065			4852
	1.7681			4852
	1.77603			4852
	1.78455			4852
	1.79378			4852
	1.80382			4852
	1.81458			4852
	1.82585			4852
	1.8374			4852
1.84926	4852			
1.86171	9704			
1.87511	4852			
1.89	4852			

Table D.4: Simulation parameters for $L = 6$, $B_x = 0.0$, without ODD terms

L	T	N_{mc}	N_{eq}	N_{eff}
6	1.69	363000	131071	1811
	1.69635			1811
	1.70263			905
	1.70886			905
	1.71508			905
	1.72131			905
	1.72756			905
	1.73386			905
	1.74026			905
	1.7468			452
	1.75357			905
	1.76065			905
	1.7681			905
	1.77603			905
	1.78455			905
	1.79378			905
	1.80382			905
	1.81458			905
	1.82585			452
	1.8374			452
1.84926	905			
1.86171	1811			
1.87511	905			
1.89	905			

Table D.5: Simulation parameters for $L = 4$, $B_x = 0.3$, without ODD terms

L	T	N_{mc}	N_{eq}	N_{eff}
4	1.67	2097152	32767	4032
	1.67661			2016
	1.68313			8064
	1.6896			8064
	1.69607			8064
	1.70255			8064
	1.70905			8064
	1.71558			8064
	1.72217			8064
	1.72886			8064
	1.73568			8064
	1.7427			8064
	1.75			8064
	1.75765			8064
	1.76573			16128
	1.77427			8064
	1.78333			8064
	1.79299			8064
	1.80337			16128
	1.81464			16128
	1.82698			16128
	1.84038			16128
	1.85475			16128
1.87	16128			

Table D.6: Simulation parameters for $L = 5$, $B_x = 0.3$, without ODD terms

L	T	N_{mc}	N_{eq}	N_{eff}
5	1.67	1191000	262143	7256
	1.67661			3628
	1.68313			3628
	1.6896			1814
	1.69607			7256
	1.70255			1814
	1.70905			3628
	1.71558			3628
	1.72217			3628
	1.72886			1814
	1.73568			3628
	1.7427			3628
	1.75			7256
	1.75765			3628
	1.76573			7256
	1.77427			3628
	1.78333			1814
	1.79299			3628
	1.80337			1814
	1.81464			1814
	1.82698			1814
	1.84038			7256
	1.85475			7256
	1.87			7256

Table D.7: Simulation parameters for $L = 6$, $B_x = 0.3$, without ODD terms

L	T	N_{mc}	N_{eq}	N_{eff}
6	1.67	328500	32767	2310
	1.67661			2310
	1.68313			2310
	1.6896			2310
	1.69607			2310
	1.70255			2310
	1.70905			1155
	1.71558			1155
	1.72217			577
	1.72886			1155
	1.73568			1155
	1.7427			1155
	1.75			1155
	1.75765			1155
	1.78333			1155
	1.79299			1155
	1.80337			1155
	1.81464			1155
	1.82698			1155
	1.84038			577
1.85475	1155			
1.87	577			

Table D.8: Simulation parameters for $L = 4$, $B_x = 0.0$, with ODD terms

L	T	N_{mc}	N_{eq}	N_{eff}
4	1.44	2097152	1048575	8192
	1.4474			8192
	1.45477			8192
	1.46213			8192
	1.46949			8192
	1.47688			8192
	1.48431			8192
	1.49179			4096
	1.49933			4096
	1.50695			4096
	1.51468			4096
	1.52254			8192
	1.53054			8192
	1.53874			4096
	1.54715			4096
	1.55581			4096
	1.56478			4096
	1.5741			8192
	1.58383			8192
	1.59401			8192
	1.60469			4096
	1.61589			4096
	1.62764			4096
1.64	8192			

Table D.9: Simulation parameters for $L = 5$, $B_x = 0.0$, with ODD terms

L	T	N_{mc}	N_{eq}	N_{eff}
5	1.5	2097152	524287	3072
	1.50638			3072
	1.51257			3072
	1.5186			3072
	1.52462			3072
	1.53075			3072
	1.53709			3072
	1.5436			3072
	1.55017			3072
	1.55676			3072
	1.56343			3072
	1.57032			3072
	1.57753			1536
	1.58512			1536
	1.59315			3072
	1.60173			1536
	1.61099			3072
	1.62104			3072
	1.63167			3072
	1.6427			3072
	1.66747			3072
1.6841	3072			
1.7	6144			

Table D.10: Simulation parameters for $L = 6$, $B_x = 0.0$, with ODD terms

L	T	N_{mc}	N_{eq}	N_{eff}
6	1.5	351000	131071	2230
	1.50638			2230
	1.51257			1115
	1.5186			2230
	1.52462			2230
	1.53075			2230
	1.53709			2230
	1.5436			1115
	1.55017			1115
	1.55676			1115
	1.56343			1115
	1.57753			1115
	1.58512			1115
	1.59315			1115
	1.60173			1115
	1.61099			1115
	1.62104			1115
	1.63167			1115
	1.6427			1115
	1.65437			1115
1.66747	1115			
1.6841	2230			
1.7	1115			

Table D.11: Simulation parameters for $L = 4$, $B_x = 0.3$, with ODD terms

L	T	N_{mc}	N_{eq}	N_{eff}
4	1.45	2097152	131071	15360
	1.45736			15360
	1.46469			7680
	1.472			7680
	1.4793			15360
	1.48661			15360
	1.49397			15360
	1.50139			7680
	1.5089			15360
	1.51652			7680
	1.52428			1920
	1.5322			7680
	1.54029			7680
	1.54856			7680
	1.55702			7680
	1.56573			7680
	1.57478			7680
	1.58422			7680
	1.59407			7680
	1.60432			7680
	1.61496			3840
1.62603	3840			
1.63768	3840			
1.65	3840			

Table D.12: Simulation parameters for $L = 5$, $B_x = 0.3$, with ODD terms

L	T	N_{mc}	N_{eq}	N_{eff}
5	1.48	1680000	8191	3265
	1.48722			3265
	1.49429			3265
	1.50119			3265
	1.50796			3265
	1.51467			3265
	1.52143			1632
	1.52839			3265
	1.53573			3265
	1.54329			3265
	1.55068			3265
	1.55774			3265
	1.56467			3265
	1.57166			3265
	1.57892			3265
	1.58669			3265
	1.59545			3265
	1.60538			3265
	1.61589			3265
	1.62658			3265
	1.63751			3265
	1.64973			6530
	1.66544			6530
	1.68			1632

Table D.13: Simulation parameters for $L = 6$, $B_x = 0.3$, with ODD terms

L	T	N_{mc}	N_{eq}	N_{eff}
6	1.48	250500	16383	1829
	1.48722			1829
	1.49429			914
	1.50119			3658
	1.50796			914
	1.51467			914
	1.52143			228
	1.52839			457
	1.53573			457
	1.54329			228
	1.55068			914
	1.55774			914
	1.56467			228
	1.57166			457
	1.57892			914
	1.58669			914
	1.59545			914
	1.60538			457
	1.61589			1829
	1.62658			914
	1.63751			1829
	1.66544			1829
	1.68			1829

Bibliography

- [1] Bitko, D., Rosenbaum, T. F., and Aeppli, G. Quantum critical behavior for a model magnet. *Phys. Rev. Lett.*, 77:940–943, 1996.
- [2] Tabei, S. M. A., Gingras, M. J. P., Kao, Y.-J., and Yavors’kii, T. Perturbative quantum monte carlo study of LiHoF_4 in a transverse magnetic field. *Phys. Rev. B*, 78:184408, 2008.
- [3] Chakraborty, P. B., Henelius, P., Kjønsgberg, H., Sandvik, A. W., and Girvin, S. M. Theory of the magnetic phase diagram of LiHoF_4 . *Phys. Rev. B*, 70:144411, 2004.
- [4] Rønnow, H. M., Jensen, J., Parthasarathy, R., Aeppli, G., Rosenbaum, T. F., McMorro, D. F., and Kraemer, C. Magnetic excitations near the quantum phase transition in the ising ferromagnet LiHoF_4 . *Phys. Rev. B*, 75:054426, 2007.
- [5] Babkevich, P., Nikseresht, N., Kovacevic, I., Piatek, J. O., Dalla Piazza, B., Kraemer, C., Krämer, K. W., Prokeš, K., Mat’áš, S., Jensen, J., and Rønnow, H. M. Phase diagram of diluted Ising ferromagnet $\text{LiHo}_x\text{Y}_{1-x}\text{F}_4$. *Phys. Rev. B*, 94:174443, 2016.
- [6] Dunn, J. L., Stahl, C., Macdonald, A. J., Liu, K., Reshitnyk, Y., Sim, W., and Hill, R. W. Testing the transverse field ising model in LiHoF_4 using capacitive dilatometry. *Phys. Rev. B*, 86:094428, 2012.
- [7] Giraud, R., Wernsdorfer, W., Tkachuk, A. M., Mailly, D., and Barbara, B. Nuclear spin driven quantum relaxation in $\text{LiY}_{0.998}\text{Ho}_{0.002}\text{F}_4$. *Phys. Rev. Lett.*, 87:057203, 2001.
- [8] Schechter, M. and Stamp, P. C. E. Derivation of the low- t phase diagram of $\text{LiHo}_x\text{Y}_{1-x}\text{F}_4$: A dipolar quantum ising magnet. *Phys. Rev. B*, 78:054438, 2008.

- [9] Gingras, M. J. P. and Henelius, P. Collective phenomena in the $\text{LiHo}_x\text{Y}_{1-x}\text{F}_4$ quantum ising magnet: Recent progress and open questions. *Journal of Physics: Conference Series*, 320:012001, 2011.
- [10] Tabei, S. M. A., Gingras, M. J. P., Kao, Y.-J., Stasiak, P., and Fortin, J.-Y. Induced random fields in the $\text{LiHo}_x\text{Y}_{1-x}\text{F}_4$ quantum ising magnet in a transverse magnetic field. *Phys. Rev. Lett.*, 97:237203, 2006.
- [11] Schechter, M. and Laflorencie, N. Quantum spin glass and the dipolar interaction. *Phys. Rev. Lett.*, 97:137204, 2006.
- [12] Schechter, M. $\text{LiHo}_x\text{Y}_{1-x}\text{F}_4$ as a random-field ising ferromagnet. *Phys. Rev. B*, 77:020401, 2008.
- [13] Hansen, P. E., Johansson, T., and Nevald, R. Magnetic properties of lithium rare-earth fluorides: Ferromagnetism in LiErF_4 and LiHoF_4 and crystal-field parameters at the rare-earth and li sites. *Phys. Rev. B*, 12:5315–5324, 1975.
- [14] Biltmo, A. and Henelius, P. Phase diagram of the dilute magnet $\text{LiHo}_x\text{Y}_{1-x}\text{F}_4$. *Phys. Rev. B*, 76:054423, 2007.
- [15] Silevitch, D., Bitko, D., Brooke, J., Ghosh, S., Aeppli, G., and Rosenbaum, T. A ferromagnet in a continuously tunable random field. *Nature*, 448(7153):567, 2007.
- [16] Schechter, M. and Stamp, P. C. E. Significance of the hyperfine interactions in the phase diagram of $\text{LiHo}_x\text{Y}_{1-x}\text{F}_4$. *Phys. Rev. Lett.*, 95:267208, 2005.
- [17] Press, W. H., Teukolsky, S. A., Vetterling, W. T., and Flannery, B. P. *Numerical Recipes 3rd Edition: The Art of Scientific Computing*. Cambridge University Press, New York, NY, USA, 2007.
- [18] Newman, M. and Barkema, G. *Monte Carlo Methods in Statistical Physics*. Clarendon Press, 1999.
- [19] Katzgraber, H. G., Körner, M., and Young, A. P. Universality in three-dimensional ising spin glasses: A monte carlo study. *Phys. Rev. B*, 73:224432, 2006.
- [20] Flyvbjerg, H. and Petersen, H. G. Error estimates on averages of correlated data. *The Journal of Chemical Physics*, 91(1):461–466, 1989.

- [21] Ambegaokar, V. and Troyer, M. Estimating errors reliably in monte carlo simulations of the ehrenfest model. *American Journal of Physics*, 78(2):150–157, 2010.
- [22] Andresen, J. C., Thomas, C. K., Katzgraber, H. G., and Schechter, M. Novel disordering mechanism in ferromagnetic systems with competing interactions. *Phys. Rev. Lett.*, 111:177202, 2013.
- [23] Ashcroft, N. and Mermin, N. *Solid State Physics*, pages 122–123, 643–657. Harcourt College Publishers, New York, 1976.
- [24] Hutchings, M. Point-charge calculations of energy levels of magnetic ions in crystalline electric fields. volume 16 of *Solid State Physics*, pages 227 – 273. Academic Press, 1964.
- [25] Prather, J. L. Atomic energy levels in crystals. Monograph 19, U.S. Department of Commerce, National Bureau of Standards, 1961.
- [26] Stevens, K. W. H. Matrix elements and operator equivalents connected with the magnetic properties of rare earth ions. *Proceedings of the Physical Society. Section A*, 65(3):209–215, 1952.
- [27] de Leeuw, S. W., Perram, J. W., Smith, E. R., and Rowlinson, J. S. Simulation of electrostatic systems in periodic boundary conditions. i. lattice sums and dielectric constants. *Proceedings of the Royal Society of London. A. Mathematical and Physical Sciences*, 373(1752):27–56, 1980.
- [28] Wang, Z. and Holm, C. Estimate of the cutoff errors in the ewald summation for dipolar systems. *The Journal of Chemical Physics*, 115(14):6351–6359, 2001.
- [29] De Leeuw, S., Perram, J. W., and Smith, E. Computer simulation of the static dielectric constant of systems with permanent electric dipoles. *Annual review of physical chemistry*, 37(1):245–270, 1986.